Predicting the X-ray polarization of type-2 Seyfert galaxies

F. Marin, M. Dovciak, F. Muleri, F.F. Kislat, H.S. Krawczynski

Monthly Notices
of the
ROYAL ASTRONOMICAL SOCIETY

MNRAS **473,** 1286–1316 (2018)
Advance Access publication 2017 September 13

doi:10.1093/mnras/stx2382

Predicting the X-ray polarization of type 2 Seyfert galaxies

F. Marin,[1⋆] M. Dovčiak,[2] F. Muleri,[3] F. F. Kislat[4] and H. S. Krawczynski[4]

[1]*Observatoire Astronomique de Strasbourg, Université de Strasbourg, CNRS, UMR 7550, 11 rue de l'Université, F-67000 Strasbourg, France*
[2]*Astronomical Institute of the Academy of Sciences, Boční II 1401, CZ-14100 Prague, Czech Republic*
[3]*INAF/IAPS, Via del Fosso del Cavaliere 100, I-00133 Roma, Italy*
[4]*Physics Department and McDonnell Center for the Space Sciences, Washington University in Saint Louis, Saint Louis, MO 63130, USA*

Accepted 2017 September 11. Received 2017 September 11; in original form 2017 July 25

ABSTRACT

Infrared, optical and ultraviolet spectropolarimetric observations have proven to be ideal tools for the study of the hidden nuclei of type 2 active galactic nuclei (AGN) and for constraining the composition and morphology of the sub-parsec scale emission components. In this paper, we extend the analysis to the polarization of the X-rays from type 2 AGN. Combining two radiative transfer codes, we performed the first simulations of photons originating in the gravity-dominated vicinity of the black hole and scattering in structures all the way out to the parsec-scale torus and polar winds. We demonstrate that, when strong gravity effects are accounted for, the X-ray polarimetric signal of Seyfert-2s carries as much information about the central AGN components as spectropolarimetric observations of Seyfert-1s. The spectropolarimetric measurements can constrain the spin of the central supermassive black hole even in edge-on AGN, the hydrogen column density along the observer's line-of-sight and the composition of the polar outflows. However, the polarization state of the continuum source is washed out by multiple scattering, and should not be measurable unless the initial polarization is exceptionally strong. Finally, we estimate that modern X-ray polarimeters, either based on the photoelectric effect or on Compton scattering, will require long observational times on the order of a couple of megaseconds to be able to properly measure the polarization of type 2 AGN.

Key words: polarization – radiative transfer – relativistic processes – scattering – galaxies: active – X-rays: general.

1 INTRODUCTION

Most, if not all, galaxies contain at least one supermassive black hole (SMBH) at their centre, although not all of them show as dramatic observational signatures as quasars. In the case of long and steady accretion, the central SMBH can enter a phase where the viscosity of the accreting matter can lead to emission outshine the entire host galaxy (Pringle & Rees 1972; Shakura & Sunyaev 1973). This type of object is called an active galactic nuclei (AGN) and typically stays in an accretion-efficient state for about 10^5 yr before returning to a quiescent phase (Schawinski et al. 2015). The AGN lifetime is short compared to the total growth time of a galaxy but quasars strongly impact their host galaxy during that period. By studying AGN, we can understand how the feedback mechanism, i.e. the material expelled by radiation, winds and jets from the vicinity of the potential well, can affect its host galaxy in less than a million years. Springel et al. (2005), Nandra et al. (2007), Schawinski et al. (2009) and other authors have found that quenching star formation from AGN feedback could move the host galaxy from a blue (star-forming) to a passive (red sequence) galaxy classification. Additionally, the mass of the central SMBH in nearby galaxies was found to correlate with the host bulge luminosity (McLure, Dunlop & Kukula 2000), velocity dispersion (Ferrarese & Merritt 2000; Gebhardt et al. 2000) and mass (Magorrian et al. 1998). Hence, to understand the evolution of galaxies, exploring the AGN phase is of utmost importance.

According to the standard paradigm, all AGN are relatively similar in terms of physics but several key parameters such as orientation (Marin 2014, 2016), mass accretion rate (Meier 2002; Fanidakis et al. 2011) and feedback (Kauffmann & Haehnelt 2000; Fabian 2012) can differ, resulting in a zoo of active galaxy classes (Antonucci 1993; Urry & Padovani 1995). It is still unclear which of the aforementioned three parameters is the main driver in the unification scheme and a detailed multiwavelength investigation of nearby AGN is mandatory to draw a self-consistent picture.

The X-ray band is particularly well suited for the exploration of the AGN physics and constituents. X-ray radiation is produced

⋆ E-mail: frederic.marin@astro.unistra.fr

close to the central SMBH by inverse Compton scattering of thermally emitted ultraviolet photons in a corona situated above the disc (Haardt & Maraschi 1991, 1993). This corona of hot electrons becomes the central continuum source of a power-law emission that will illuminate the innermost regions of the accretion flow. Observing the X-ray light after absorption, re-emission and scattering inside the compact nuclei will provide crucial information about the localization, density and composition of gaseous and dusty media along the observer's line-of-sight (e.g. Winter et al. 2009; Buchner et al. 2015). Imprinted on the X-ray spectra are the signatures of cold or ionized atoms, informing us about the velocities of unresolvable AGN components, together with the ionization fraction and intrinsic temperature (e.g. Porquet & Dubau 2000; Tombesi et al. 2010, 2013). Finally, reprocessing will lead to strong constraints on the morphology and composition of the scattering media, hidden in the polarization of the X-ray light (Matt, Fabian & Ross 1993). The observed X-ray polarization fraction and angle depend on the curved trajectories and the scattering of the photons in the vicinity of the black hole (Dovčiak et al. 2004; Schnittman & Krolik 2009) and on the structure and strength of the magnetic fields in the accretion flow (McNamara, Kuncic & Wu 2009) and thus give additional information to that obtainable through the spectroscopic and timing channels.

It has been 50 yr since the pioneering X-ray experiments on cosmic sources (Giacconi et al. 1962; Giacconi, Gursky & Waters 1964). Both X-ray spectroscopy and timing techniques are now mature and well established but, in this regard, X-ray polarization is far behind. The only dedicated high-sensitivity X-ray polarimetry mission was launched in the 1970s (Novick et al. 1972; Weisskopf et al. 1976, 1978), and proposed follow-up missions based on Bragg and Thomson/Compton scattering were not selected for implementation. The *8th Orbiting Solar Observatory* (*OSO-8*) mission achieved only one highly significant (19σ) detection of the X-ray polarization of the Crab nebula and a handful of 99 per cent confidence upper limits on additional compact X-ray sources were acquired before the X-ray polarimetric technology became no longer competitive compared to other investigation techniques (Weisskopf 2010). We had to wait for the development of new instruments relying on non-rotating photoelectric polarimeter in the early 2000s to revive the field (Costa et al. 2001). Combining new gas pixel and Compton scattering detectors with focusing X-ray optics improved by a factor of 100 the sensitivity of X-ray polarimeters with respect to the old generation of instruments, opening a new observational window for the high-energy sky (Bellazzini et al. 2006, 2007). Two balloon-borne instruments, relying on scattering polarimetry, have flown in the recent years: X-Calibur (see Beilicke et al. 2012, 2014; Krawczynski et al. 2016a) and PoGO-Lite (see Kamae et al. 2008; Pearce 2012; Chauvin et al. 2016). The first X-ray mission to fly a photoelectric imaging polarimeter in space will be launched by NASA in 2020 (Weisskopf et al. 2016). It is thus necessary to prepare the ground and to begin to refine the theories and simulations for interpreting the observational results to come.

X-ray polarimetric simulations of AGN have been presented in several key papers that can be divided into two groups: either the simulations were focusing on the central SMBH and its accretion disc, excluding any reprocessing regions farther than a thousand of gravitational radii (Dovčiak et al. 2008; Schnittman & Krolik 2009, 2010; Hoormann, Beheshtipour & Krawczynski 2016), or the models did not account for relativistic effects (Matt et al. 1989; Marin et al. 2012a, 2013; Marin, Goosmann & Petrucci 2016). The propagation of photons through the curved space–time of rotating black holes, referred to as 'strong gravity effects in the following, significantly modify the polarization of the observed radiation. In particular, the polarization angle (Ψ) as seen by an observer at infinity is rotated due to aberration and light bending effects (e.g. Connors & Stark 1977; Pineault 1977; Connors, Stark & Piran 1980). The rotation is larger for smaller radii and higher inclination angles. Introducing strong gravity effects is thus important in any X-ray polarimetric modelling of AGN but the computational time becomes significant when the code has to account for scattering, absorption and reemission of photons on parsec scales. In the case of type-1 AGN the central engine is seen from the pole, through the outflowing winds and warm absorber region (Halpern 1984). Forward scattering of high energy radiation leads to very small degrees of polarization (Marin et al. 2012a) and it is, at first order, possible to use simulations of isolated SMBH with an accretion disc to estimate the net X-ray polarization of type-1 AGN. However, in the case of type 2 objects, where the observer's line-of-sight is obscured by a dense, cold, circumnuclear medium, photons encounter multiple scattering inside the torus funnel or in the winds before escaping the AGN. The resulting polarization is expected to be high (several tens of per cents; see Marin et al. 2016). Additionally, the observations of Seyfert-2s often indicate the presence of a constant and soft emission component, commonly attributed to the scattering of X-rays by highly ionized gas, but which is not clearly separable from the more powerful torus scattering at higher energies. NGC 1068 thought to be dominated by electron scattering does not exhibit this emission component (Kinkhabwala et al. 2002; Marinucci et al. 2016), but NGC 4945 shows it very clearly (Madejski et al. 2000; Puccetti et al. 2014).

This paper focuses on the study of the polarization properties of the 1–100 keV emission of Seyfert-2s. We account for the first time for the effect of strong gravity and the photon reprocessing by various structures, such as the equatorial gaseous torus and the conical polar winds. By including strong gravity effects close to the black hole, we investigate if the rotation of polarization angle along the photon's null geodesics can be detected by an X-ray polarimeter, or if the polarization signal is washed out by multiple scattering. We also include in the code the polarization state of the continuum source and explore how the final polarization reaching the observer is affected by these modifications. As previously stated, we focus on type 2 AGN as polar scattering is needed to escape the dense circumnuclear environment of the central SMBH, leading to higher polarization degrees than for type-1 objects. The higher the polarization degree, the better are the chances for a clean measurement of its X-ray polarization (modulo the X-ray flux of the source). We present the models and the code in Section 2, discuss our outcomes in Section 3 and provide estimates of the detectability of X-ray polarization signals from type 2 AGN in Section 4. In the light of our results, we conclude in Section 5 on the feasibility of measuring polarimetric signatures imprinted with general relativistic effects and/or physical characteristics of the continuum source (temperature, density, composition...).

2 MODELLING

We model the X-ray polarization emerging from a complex AGN model by combining the general relativistic KY code with the STOKES scattering code (Goosmann & Gaskell 2007; Dovčiak et al. 2011; Marin et al. 2012b; Marin, Goosmann & Gaskell 2015). The KY code simulates the compact object, i.e. tracks photons up to a certain radius, and then STOKES takes over to propagate radiation through

the torus and polar winds. We created an AGN model following the unified scheme and included the possibility to turn on/off the strong gravity effects and the initial polarization of the coronal photons.[1]

2.1 The radiative transfer code

The emission and scattering of radiation within the first thousand gravitational radii were simulated using the updated KY code for the relativistic reflection of polarized primary radiation from a cold accretion disc (see Dovčiak et al. 2011). The code assumes that the primary source of X-ray radiation is geometrically small and located on the symmetry axis (i.e. lamp-post geometry). The primary emission, considered to be isotropic and polarized, illuminates the accretion disc below. The disc is assumed to be a Keplerian, geometrically thin, optically thick, cold disc with inner edge located at the marginally stable orbit [innermost stable circular orbit (ISCO)] determined by the spin of the central SMBH. Reprocessing in the disc is calculated with the Monte Carlo multiscattering code NOAR (Dumont, Abrassart & Collin 2000), which computes the reflected flux including the iron fluorescent Kα and Kβ lines. The single-scattering approximation (Chandrasekhar 1960) is used for the local polarization of the reflected continuum component, while the line flux is supposed to be unpolarized. Both the reflected flux from the disc and its polarization properties depend on the geometry of scattering, i.e. on the incident and emission angles and the relative azimuthal angle between incident and emitted light rays. Further, the local polarization properties of reflection depend on the polarization degree and angle of the incident illumination. A fully relativistic ray-tracing code in vacuum is used for photon paths from the corona to the disc and from corona and disc to outer parts of the system where relativistic effects are negligible. Note that the polarization direction rotates along the photon trajectory as a consequence of the polarization vector being parallel transported along the geodesic between the emission of the photon and the scattering off the disc and thus the illuminating flux has a distribution of incident polarization angles. As a consequence of all these effects, the local polarization properties of the reprocessed radiation depend on the position on the disc where it is reflected from (both radial and azimuthal). The relativistic effects further change the polarization angle as the light travels from the disc to the more distant components of the system, especially for the light coming from the innermost parts of the disc. Therefore, the polarization properties of the radiation from the inner parts of the accretion flow result from adding the polarized emission from the corona and from all parts of the accretion disc and it will depend on the relative location of the inner accretion flow and the particular distant components.

STOKES is a Monte Carlo radiative transfer code developed to study the broad-band, scattering-induced, polarization signatures of AGN (Goosmann & Gaskell 2007; Marin et al. 2012b, 2015). The code can handle a large variety of geometrical structures arranged around the continuum source and accounts for all the reprocessing mechanisms from the near-infrared to the hard X-ray bands. Multiple scattering allows the radiative coupling between all the AGN components and, once radiation has escaped the model, it is recorded by a spherical web of virtual detectors, allowing to compute the intensity and polarization spectra for all polar and azimuthal angles at once. Special and general relativity are not included in STOKES, hence the use of the input data from KY. The scattering code samples photons according to the flux distribution from KY, including the polarization state of radiation and its direction of propagation. In this paper, we neglect magnetic field effects and limit the modelling to radio-quiet Seyfert galaxies. A manual for the utilization of STOKES can be found online (http://www.stokes-program.info), together with a free version of the code working in the optical and ultraviolet bands.

[1] For the remainder of this paper, the term 'primary' emission will refer to the coronal emission.

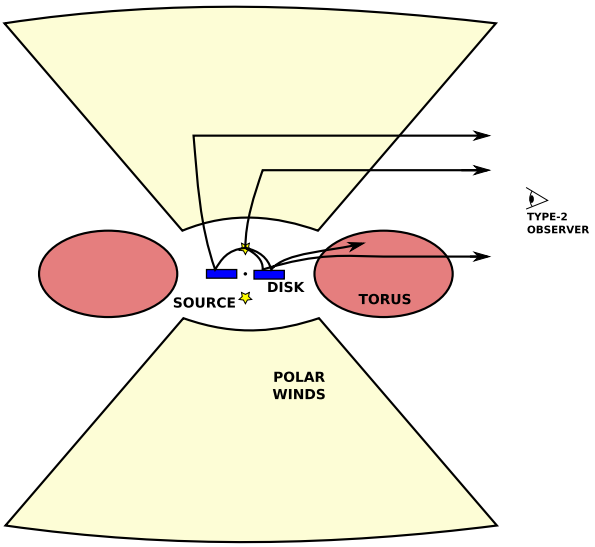

Figure 1. Artist representation of the AGN model. Scales have been exaggerated for better visualization of the inner components. The point-like coronas are represented with yellow stars, the cold accretion disc is in blue, the gaseous torus in red and the polar outflows in primrose yellow. The photon trajectories are bend close to the central SMBH. Photons can scatter inside the polar winds to reach the observer or, depending upon the energy of radiation and Compton thickness of the equatorial material, can pass through the gas.

2.2 The AGN model

We followed the geometrical depiction of AGN from Antonucci (1993) to construct our baseline model (see Fig. 1). This model consists of a central SMBH surrounded by a geometrically thin accretion disc. The disc is irradiated by two compact coronas situated above and below the disc emitting the X-ray photons irradiating the accretion disc. Along the equatorial plane, at a parsec-scale distance is a compact gaseous torus that blocks radiation and collimates a conical wind that extends towards the polar region.

The black hole mass distribution observed in large radio-quiet Seyfert catalogues is quite narrow, with an average mass of $\sim 10^8\,M_\odot$ (Woo & Urry 2002), so we fixed the mass of our SMBH to the same value. We allowed the spin of the black hole to be either 0 (Schwarzschild case) or 1 (Kerr black hole). The dimensionless spin parameter gives the angular momentum of the black hole and impacts the location of the innermost stable circular orbit and thus the inner edge of the accretion disc. The more rapidly the black hole spins, the closer the accretion disc extends towards the black hole, and the stronger are the general relativistic effects (see e.g. Dovčiak et al. 2011).

Our black hole is surrounded by a geometrically thin (radius $\gg$ height), optically thick (electron optical depth > 1) accretion disc filled with neutral matter with solar abundances and composition. X-ray photons are emitted by a compact source with a height of

3 gravitational radii and situated in a lamp-post geometry (i.e. on the disc symmetry axis). The photon index Γ is equal to 2, where $N(E) \propto E^{-\Gamma}$ and $\alpha = -(\Gamma - 1)$. This power-law photon index has been chosen accordingly to the observed indexes measured in different AGN samples, with typical values lying between 1.5 and 2.5 (e.g. Nandra & Pounds 1994; Page et al. 2005). We set the continuum source to radiate photons in the 1–100 keV band, with either an unpolarized corona emission, or a polarized primary with a 2 per cent linear polarization. The polarized primary can have two different configurations: either perpendicular or parallel. Polarization is described as parallel when its electric vector is aligned with the projected symmetry axis of the model (polarization position angle $\Psi = 90^\circ$). In the case of orthogonality, the polarization is described as perpendicular ($\Psi = 0^\circ$). We estimate the polarization from the Comptonization of the photons in the corona with the classical result for scattering-dominated atmospheres presented in Chandrasekhar (1960).

At larger distances from the central engine is an obscuring circumnuclear cold matter torus. The torus extends from 0.01 pc from the centre of the model to 5 pc. The inner radius has been set accordingly to the mass and luminosity of the central SMBH (Suganuma et al. 2006) and the outer radius is consistent with the maximum extension of the circumnuclear dusty torus as observed/modelled in the infrared (Fritz, Franceschini & Hatziminaoglou 2005; Siebenmorgen, Heymann & Efstathiou 2015). Its half-opening angle is set to 60° from the polar axis, so that the line-of-sight of an observer situated along the equatorial plane (a type 2 view) is obscured by the gaseous medium. We assume three different amounts of hydrogen column densities along the observer's line-of-sight: 10^{23}, 10^{24} or 10^{25} atm cm^{-2}. By doing so, we model both Compton-thin and Compton-thick AGN classes (with the transition between Compton-thin and Compton-thick Seyferts starting at 10^{24} atm cm^{-2}; see Risaliti et al. 2005).

Finally, along the pole, we added the possibility to have an outflowing wind, collimated by the torus funnel. The wind extends 60° from the polar axis, and it is either composed of neutral gas in a Compton-thin regime, or filled with electrons only (radial optical depth much lower than unity). The wind base is located at a radial distance of 0.1 pc from the centre of the model and extends up to 25 pc, before mixing with the interstellar medium. In total, there are three kind of AGN: models without polar winds, models with low-density, cold, gaseous winds and models with a highly ionized outflow.

We thus developed a baseline model with a variety of input parametrizations in order to explore different kinds of radio-quiet AGN: from Compton-thin to Compton-thick type 2s, AGN with a maximally or non-rotating black hole, AGN lacking outflowing signatures, AGN with winds dominated by electron or neutral gas and AGN with unpolarized or partially polarized corona emission.

2.3 Polarization of the continuum source

Schnittman & Krolik (2010) and Schnittman & Krolik (2013) derived the polarization of the corona self-consistently for the case of stellar-mass black holes but the intrinsic polarization of the primary radiation was never properly calculated for AGN. Such polarization is expected to occur if the primary spectrum emitted by the lamp-post is indeed due to inverse Compton scattering of ultraviolet photons thermally emitted by the accretion disc. However the exact degree and polarization position angle resulting from this kind of interaction in the vicinity of a potential well was never investigated for the quasar class. Here we upgraded the KY code (Dovčiak et al., in preparation) to account for a non-null polarization of the corona emission.

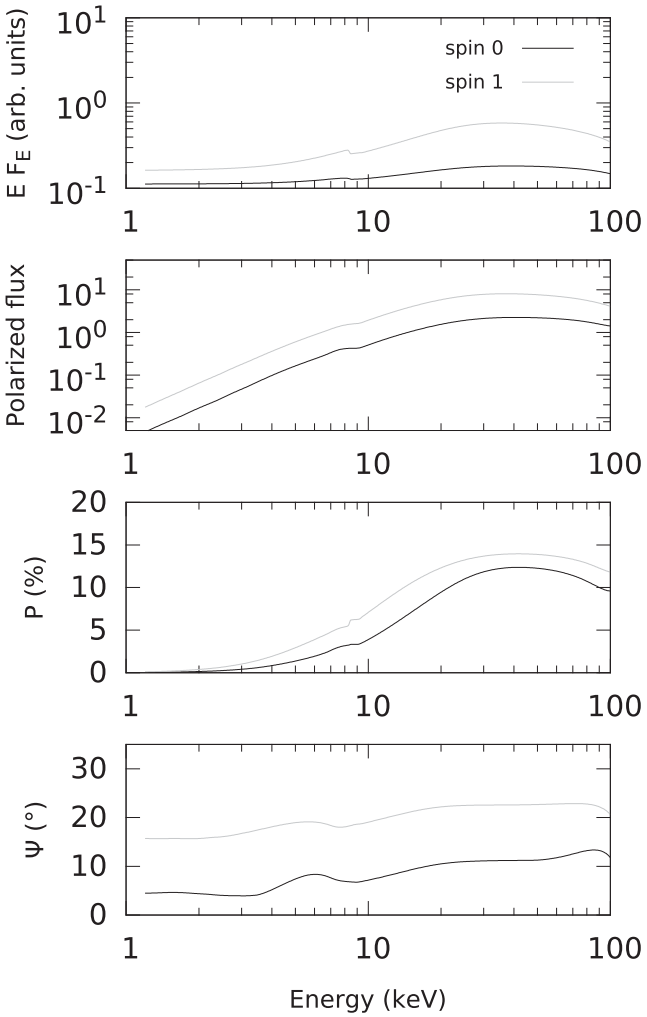

Figure 2. X-ray flux (F_E is energy flux at energy E), polarized flux ($E F_E$ times the polarization fraction), polarization degree P and polarization position angle Ψ seen by an observer at infinity, resulting from an elevated point-like corona that irradiates an accretion disc inclined by 70°. The source is unpolarized. The variation in P and Ψ is due to general relativistic effects that will induce a parallel transport of the polarization angle along geodesics, plus the scattering and re-emission of photons from the cold accretion matter. Two flavours of black holes are shown: a non-spinning Schwarzschild black hole (black line) and a maximally spinning Kerr black hole (grey line).

2.3.1 *Benchmark case: unpolarized primary*

In Fig. 2, we plot the X-ray flux, polarized flux, polarization degree P and polarization position angle Ψ seen by an observer at infinity, resulting from our baseline model without the torus and polar winds. We fixed the inclination of the observer to 70° (type 2 view) and explored two flavours of SMBH: a non-spinning Schwarzschild black hole and a maximally spinning Kerr black hole. We first examine a model where the source emits unpolarized photons. As we can see from Fig. 2 (top panel), the X-ray spectra of the two black hole systems are different in terms of intensity, the Kerr black hole re-emitting more photons that the non-spinning one. This is due to the radius of the innermost stable circular orbit that is six times smaller in the former case, allowing radiation to scatter from

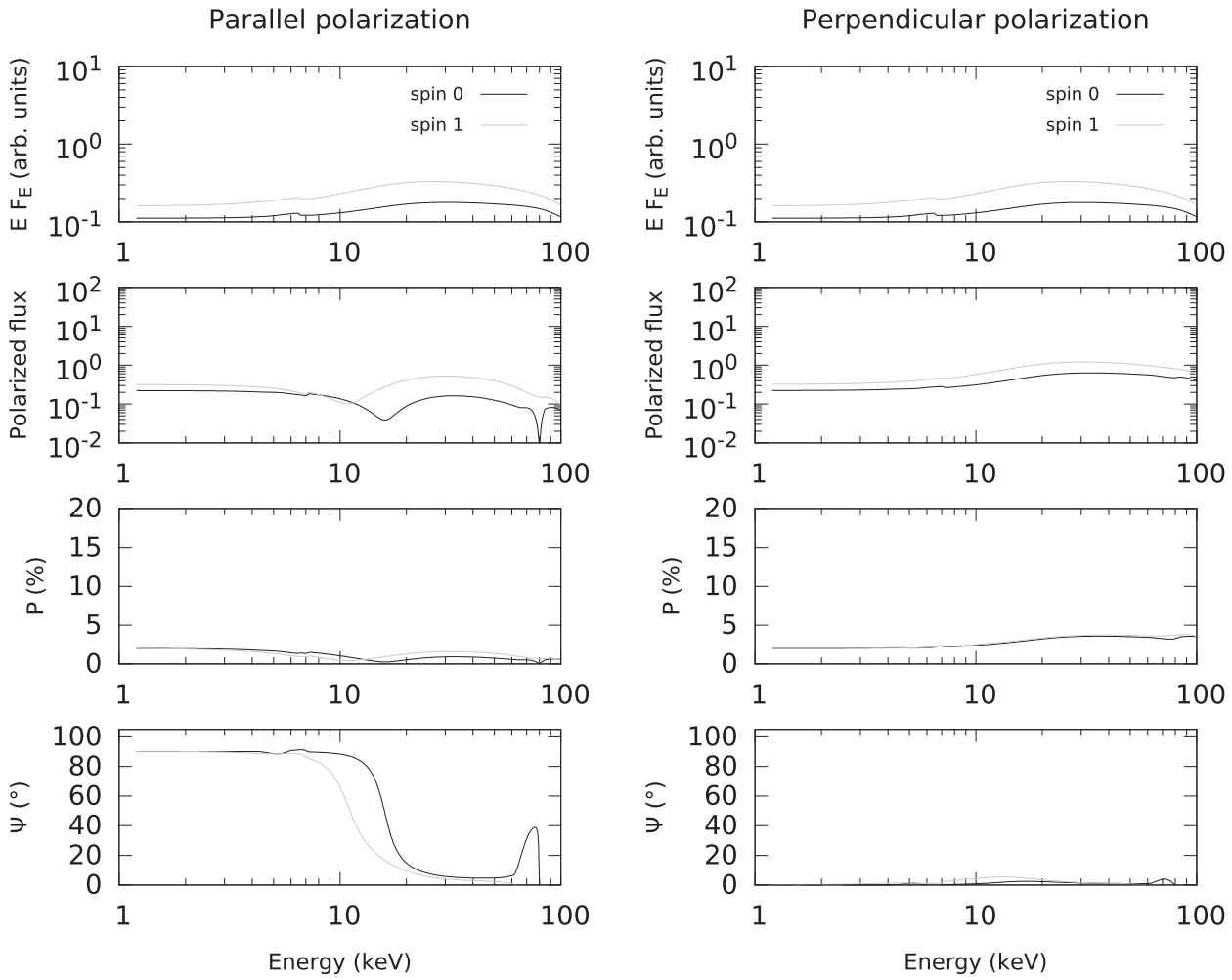

Figure 3. X-ray flux (F_E is energy flux at energy E), polarized flux (E F_E times the polarization fraction), polarization degree P and polarization position angle Ψ seen by an observer at infinity, resulting from an elevated point-like corona that irradiates an accretion disc inclined by 20°. The initial polarization is set to 2 per cent with a parallel or a perpendicular polarization angle (left and right column, respectively). The variation in P and Ψ are due to general relativistic effects that will induce a parallel transport of the polarization angle along geodesics, plus the scattering and reemission of photons from the cold accretion matter. Two flavours of black holes are shown: a non-spinning Schwarzschild black hole (black line) and a maximally spinning Kerr black hole (grey line).

the disc towards the observer, rather than crossing the event horizon in the case of a Schwarzschild black hole. The polarized flux is the multiplication of the intensity times the polarization degree. Since both the flux and P are higher for a spinning black hole, the polarized flux of a Kerr SMBH is also higher. Finally, the light bending aberration effects drive Ψ to a different value for the two black hole flavours, as the radius of the photon orbit decreases when the black hole spin increasing.

2.3.2 *Polarized primary*

We now switch on the polarization of the corona emission and investigate two configurations: either the initial polarization position angle is equal to 90° (parallel with respect to the disc axis) or $\Psi = 0°$ (perpendicular polarization). We compute the net polarization at infinity, which is a combination of direct light and photons that have scattered on to the disc surface, and present the outcomes of the simulations for two observer's inclinations: 20° and 70°.

Fig. 3 shows our results for a type-1 viewing angle (i.e. inclination of 20°). The left-hand column has an initial 2 per cent parallel polarization, and the right-hand column has a 2 per cent perpendicular polarization angle. The intensity spectra are exactly the same for both configuration of the primary polarization, indicating that spectroscopy would be insensitive to two different emission mechanisms that would mimic a compact source dominated by Compton scattering processes. Polarization, however, carries more information about the physical state of the emitting corona. If the polarization degree is twice lower than in the case of an unpolarized corona emission, with $P < 5$ per cent in both cases (and for both spin parametrization), it is primarily due to inclination (here 20° and 70° in the previous case). Polarization is sensitive to the geometry of the flow near the inner-disc boundary and decreases for larger inclinations (see Dovčiak et al. 2004). A second, less critical, depolarization effect is due to the initial polarization angle of radiation. We focus on the Kerr black hole for the following explanation, keeping in mind that the Schwarzschild case is similar. Assuming unpolarized corona emission, the net signal emerging from the accreting Kerr black hole has a net polarization direction angle of 15°–20° from 1 to 100 keV; see Fig. 2. However, if the corona emission is polarized, P will only increase if the polarization vectors have a similar Ψ; otherwise the two polarization will cancel each other, resulting in a lower P. From Fig. 3 (bottom panel), we can see

that Ψ is almost zero for all the energy bins in the case of a corona emission with perpendicular polarization (i.e. 0°), and changes from 90° to 0° in the case of a parallel initial polarization (i.e. 90°). This reinforces the decrease of P with respect to the unpolarized case. It is interesting to note that, if the corona emission imposes its initial polarization state to the signal seen by an observer at infinity in the low-energy band ($E \leq 10$ keV), at higher energies scattering from the disc will force the polarization angle to another value (shaped by special and general relativistic effects). This is due to the fact that, at low energies, photons are preferentially absorbed by the disc (with the potential re-emission of fluorescent lines) and photons reaching the observers are mostly the ones that escaped the model without scattering, hence a P close to the initial value. At higher energies, scattering from the disc dominates and P can rise. Finally, for both configuration of the initial polarization, one can see two variations of Ψ at soft (∼6–7 keV) and at high (above 60 keV) energies: in some cases relativistic effects may cause sudden changes in flux with energy to be visible in the polarization signal. This is due to the energy shift of the locally emitted spectrum due to Doppler effect and gravitational redshift. Total flux and polarization at a given energy have contributions from nearby energy bins according to energy shifts that vary across the accretion disc. Thus if there is a drop in flux, the contributions from those parts of the disc where the relativistic energy shift pushes lower flux part to certain energy will contribute less to the overall polarization properties. This can have several outcomes for the total polarization properties at this energy when compared to the energies farther away from the flux drop.

(i) Increase of polarization: the lower flux contribution parts of the disc provide varied polarization angles, and thus their depolarizing contribution to given energy is decreased due to the drop in flux.

(ii) Decrease of polarization: the lower flux contribution parts of the disc provide substantial contribution with similar polarization angles as the resultant one, and thus their polarization contribution is missing at given energy due to the drop in flux.

(iii) Fluctuation in polarization properties: a combined effect of the two above where lower flux polarization contributions may depend on the energy shift.

(iv) No effect: the lower flux contribution parts of the disc do not contribute substantially to the overall polarization, neither by depolarizing nor strengthening the polarization.

In some cases we can see these (subtle) effects around iron edge energy (7.3 keV) or at high energies where the flux decreases quickly above the Compton hump (above 60 keV). The effect appears clearly in the case of a disc inclination of 20° (Fig. 3) where for extremely spinning black hole there is an increase in polarization above 80 keV (case number 1 from the above list) and for non-rotating black hole there is a fluctuation in polarization properties at these energies (case 3 above). One should also note that the sharp cut-off for the reprocessed flux above 100 keV might also artificially impact the last energy bins. However, as it will be demonstrated in Section 3, this will have no influence on the modelling results.

In Fig. 4, the intensity and polarization spectra are shown for an inclination of 70°. Again, there is no difference between models with parallel, perpendicular or even no polarization of the corona emission in terms of spectroscopy. However, the polarization degree and polarization angle are rather different. Comparing simulations at similar observer's inclinations, the model without primary polarization shows a much lower polarization degree in the low-energy band, where absorption processes dominates. Since most of the escaping photons have travelled from the source to the observer without scattering, they carry the information about the initial polarization. This is why P is about 2 per cent below 4 keV, and has the same Ψ than the source. However, as seen from a lower inclination, the polarization position angle rotates as soon as scattering from the disc becomes efficient. The energy at which the rotation occurs depends on the spin parameter, related to the location of the innermost stable circular orbit. Since the accretion disc gets closer to the potential well for maximally spinning black holes, the polarization angle variation occurs sooner in terms of energies. The difference between the two flavours of black holes is very easy to spot between the soft and high energy band, as predicted by Schnittman & Krolik (2009, 2010), but we see here that the polarization of the corona emission can change both the value of P and the energy at which the Ψ rotation will happen.

In conclusion, for an isolated system of a SMBH plus an accretion disc, including the polarization of the corona emission will have a drastic impact on to the degree of polarization in the low-energy band, and can cause the polarization position angle to have a large amplitude variation at an energy that depends on the spin parameter. The polarization angle of the initial photons can lead Ψ observed at infinity to have an orthogonal rotation, facilitating the discrimination between different theoretical models of X-ray reprocessing in the vicinity of a compact object.

3 RESULTS

We ran the code STOKES, using the relativistic results of KY as an input parametrization of the light reprocessed by the accretion disc in the strong gravity regime. We explored a set of 81 models (with and without strong gravity effects, unpolarized or polarized corona emission, two sets of different initial polarization, three different hydrogen column densities of the torus and three parametrizations of the outflows). Each model took approximately 192 h on the platforms for intensive computing at the meso-center of the University of Strasbourg. The total amount of CPU time allocated for this research was 15 552 h, corresponding to 21 months, but reduced down to 3 months of real time continuous computation thanks to computer parallelism.

Since our principal interest is to look at the polarimetric signatures of type 2 Seyferts, for the remainder of this paper we fixed the observer's viewing angle to 70°. All the spectra of this intensive program are presented in the appendix section to improve the readability of the paper. A plot synthesizing our results is presented in Fig. 5. In the following subsections, we will describe the main outcomes from our simulations, organized as follow: first our results for an unpolarized corona emission, then for a 2 per cent parallel polarized primary and later for a 2 per cent perpendicular polarized primary.

3.1 Results for an unpolarized primary without strong gravity effects

We display our results for a type 2 AGN model without strong gravity effects and for an unpolarized source in three figures in the appendix. The first, Fig. A1, presents an AGN where the polar winds are dominated by cold material. There are three subfigures: top-left is for a torus hydrogen column density of 10^{23} atm cm^{-2} along the observer's line-of-sight, top-right for 10^{24} atm cm^{-2} and bottom for 10^{25} atm cm^{-2}. This configuration will be the same for the remainder of the figures in appendix. We see that the amount of absorbing material shapes the intensity spectra such as expected from typical modelling of type 2 AGN, see e.g. Ueda (2015), with the flux at

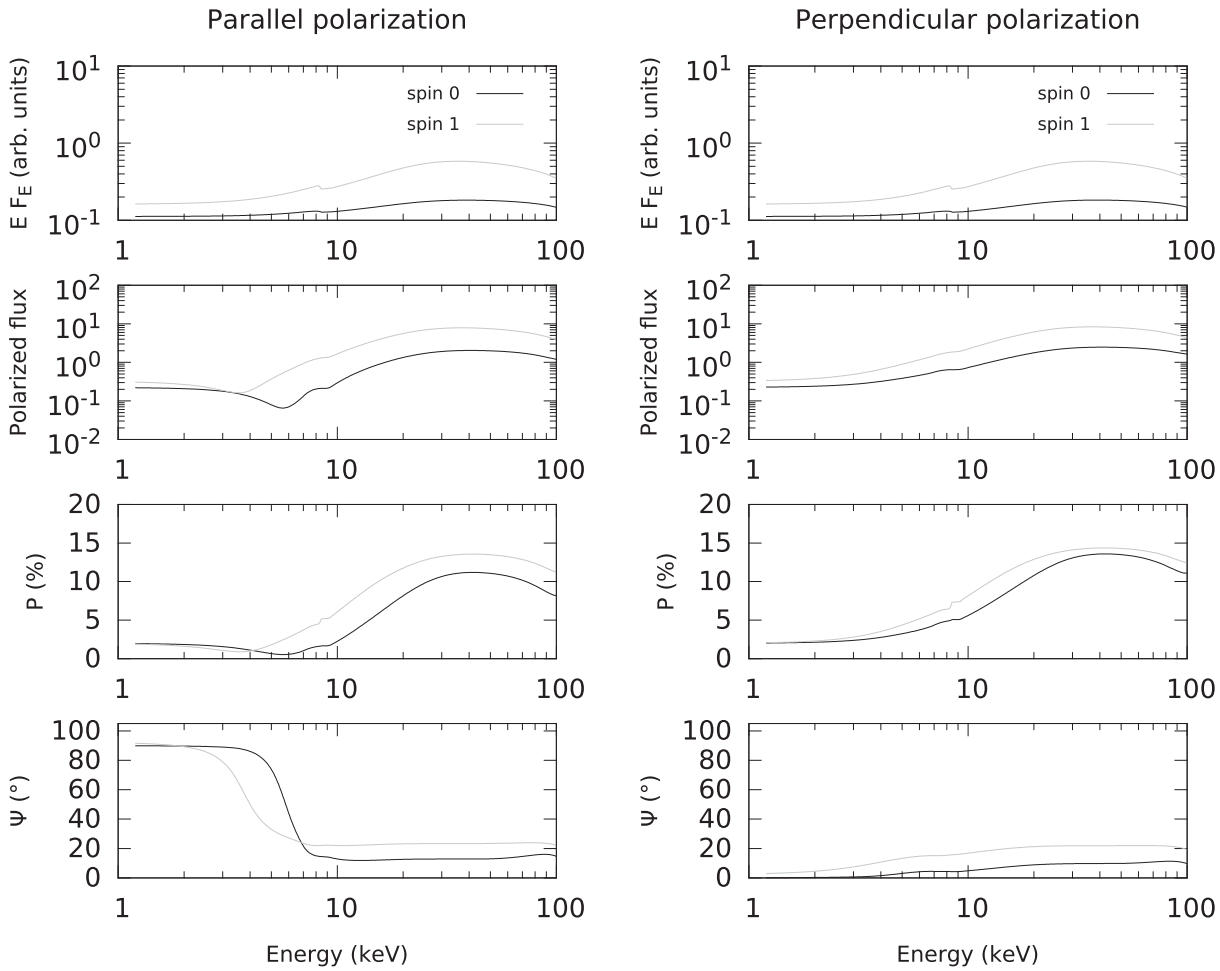

Figure 4. Same as Fig. 3, but for an accretion disc inclined by 70°.

lower energies being more suppressed by photoelectric absorption than at higher energies. It is fairly easy to differentiate Compton-thin and Compton-thick Seyfert-2s from spectroscopy, but polarization adds specific characteristics. First, the polarization degree is very high (∼30 per cent) in the soft energy band. If the hydrogen column density of the torus is too high for the low-energy photon to pass through, radiation is absorbed unless it scatters from the polar winds towards the observer. This periscope-like path is responsible for the high polarization, as orthogonal Thomson/Compton scattering produces maximum P. The composition of the wind is imprinted in the unpolarized fluorescent emission lines seen in the polarization spectra and the decrease of P indicates where photons start to leak from the equatorial plane, carrying a Ψ value of 90°. This signature also corresponds to an orthogonal rotation of the polarization position angle. It follows that the exact amount of hydrogen column density along the observer's line-of-sight can be probed with great precision by the energy at which the orthogonal switch of Ψ happens. Note that this, of course, is strongly orientation dependent. At higher energies, the polarization angle remains fixed and the increase of P with $n_{\rm H}$ is due to enhanced multiple scattering in the Compton hump.

If we compare our previous results to a model with a highly ionized, electron-filled, wind (Fig. A2), the main difference resides in the absence of signatures of fluorescent lines in the polarization spectrum for the latter case. The difference can be seen in the intensity spectra too, where the low-energy part of the spectrum is much less absorbed. It indicates that, regardless the ionization stage of the wind, if polar scattering is happening, we expect a large polarization degree at soft X-ray energies (up to 30 per cent in the case of no additional dilution). Seyfert-2s with clear electron scattering in their soft X-ray spectra are thus excellent potential targets for an X-ray polarimeter.

The case of a Seyfert-2 AGN without polar winds (a subclass of thermal AGN characterized by a very weak or absent amount of intrinsic warm absorption; see e.g. Patrick et al. 2011) is presented in Fig. A3. The lack of polar scatterers leads the intensity spectra to be very dim in the soft energy band where absorption dominates. This paucity of photons translates in polarization spectra with very poor statistics despite the large amount of computational time. The degree of polarization is lower (<20 per cent) and decreases with energy until the transition due to Compton opacity. The polarization position angle also rotates from 0° to 90° at this peculiar point and Ψ starts to stabilize. In comparison with the two other cases, a type 2 AGN without outflows would require much more observing time to get a significant X-ray polarization spectrum.

3.2 Results for an unpolarized primary with strong gravity effects

We now turn on the strong gravity effects but keep an unpolarized corona emission. The results, presented in Figs B1–B3, are now subdivided according to the dimensionless spin parameter (0 or 1).

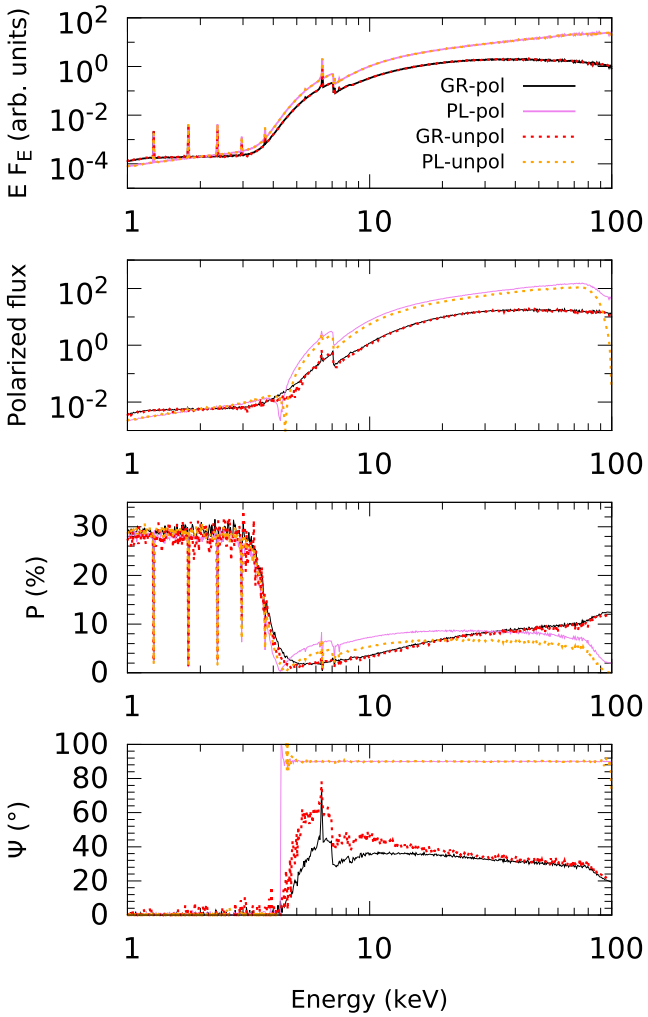

Figure 5. X-ray flux (F_E is energy flux at energy E), polarized flux ($E\,F_E$ times the polarization fraction), polarization degree P and polarization position angle Ψ seen by an observer at infinity for a Seyfert-2 AGN. The nucleus inclination is set to 70°. The model consists of two continuum sources above and below the disc irradiating a cold material, plus a circumnuclear molecular torus ($n_{\rm H_{torus}} = 10^{24}$ atm cm^{-2}) and a pair of collimated, Compton-thin, absorbing polar outflows. The four spectra show the observed fluxes and polarization for different sources (perpendicularly polarized or unpolarized power laws with/without general relativistic effects). Only one flavour of SMBH is shown (spin = 1).

For the three configurations (Compton-thin wind, ionized winds or 'bare' AGN), we find no differences in their intensity spectra between a non-rotating and a maximally rotating black hole. A spectroscopic investigation of type 2 AGN is therefore unable to distinguish between the two black hole flavours, as scattering on to the torus funnel and on the winds almost completely mask the signatures of general relativity (Streblyanska et al. 2004). The resulting narrow feature at 6.4 keV is originating from re-emission from the torus region and the extended, relativistic, red wing of the iron fluorescent emission is lost. A spectropolarimetric observation, on the other hand, provides a lot of additional information. In comparison to our previous models without strong gravity effects where the polarization position angle could only take only two values (0° and 90°), adding general relativity leads to a smooth rotation of Ψ between the soft and hard X-ray bands. The presence of winds has strong impacts. First the variation of Ψ with energy is clearly different between a cold and a highly ionized wind. The lack of polar absorption in the second case leads the polarization angle to follow the results of unpolarized light scattering off the disc (see Fig. 2), while absorption by the Compton-thin wind is more efficient to suppress the signatures of the initial polarization. X-ray polarimetry can clearly probe the composition of the outflows in this case. Second, when scattering occurs in the winds, the polarization angle of the soft X-ray radiation is naturally fixed to 0°, and at the Compton opacity transition, strong gravity effects become visible. The energy-dependent variations of the polarization position angle are directly related to the energy-dependent albedo and scattering phase function of the disc material, and help to distinguish between two different spins (Dovčiak et al. 2008, 2011). This is particularly visible for the Compton-thin cases, where the small opacity of the circumnuclear torus helps to detect the effects of strong gravity near the central SMBH. The situation is less trivial for Compton-thick type 2 Seyferts, where the difference is just a matter of a couple of degrees. This difference is completely washed out when the torus is Compton thick and collimated winds are absent (see Fig. B3).

Thereby, similarly to what we foresee for spectroscopic (Nandra et al. 1997, 2007; Yaqoob & Padmanabhan 2004) and polarimetric (Dovčiak et al. 2008; Schnittman & Krolik 2009, 2010; Marin et al. 2013) observations of type-1 AGN, measuring the X-ray polarization position angle of type 2 Seyfert galaxies will definitively tell us if strong gravity effects are important close to the central compact source, or if the signatures traditionally attributed to general relativity are in fact caused by pure absorption and Compton scattering by a distant cloudy medium (Inoue & Matsumoto 2003; Miller, Turner & Reeves 2008, 2009; Miller & Turner 2013).

3.3 Results for a 2 per cent parallel polarized primary without strong gravity effects

We now fix the polarization of the corona emission to a value of 2 per cent (linear polarization). The polarization position angle is set to 90°, i.e. parallel to the projected symmetry axis of the disc. We first investigate the resulting polarization from a polarized source without strong gravity effects.

As we can see from Figs C1–C3, the spectroscopic and polarimetric spectra are quite similar to the case of an AGN without general relativistic effects not polarized primary, with two exceptions. First the degree of polarization P is higher by about 2 per cent (corresponding to the initial P) in the hard energy band, where photons have crossed the equatorial material without suffering from heavy absorption. In the soft band, scattering off the wind material overwhelms the intrinsic primary polarization and it is impossible to identify the influence of the polarized primary. Second, the polarization position angle switch from 0° (scattering off the polar structure) to 90° (equatorial scattering) at a slightly different energy. For a type 2 AGN model with Compton-thin winds and a hydrogen column density of 10^{23} atm cm^{-2} along the observer's line-of-sight, in the case of an unpolarized corona emission the transition happens at $E = 2.1$ keV (Fig. B1, top-left case, Ψ panel), while in the case of a parallel polarized corona emission, the rotation happens at $E = 1.7$ keV (Fig. C1, top-left case, Ψ panel). This difference, marginally detectable, is the result of the input polarization matching the scattering-induced polarization from the model. Since the polarization vectors have the same Ψ, the rotation of the polarization angle is facilitated and can happen at lower energies.

We thus find that using a 2 per cent parallel polarized primary radiation enhances the observed polarization degree at high energies

and slightly alter the energy at which the orthogonal rotation of the polarization angle happens. Otherwise, the results are very similar to the ones obtained for an unpolarized corona emission in the same conditions (without strong gravity effects).

3.4 Results for a 2 per cent perpendicular polarized primary without strong gravity effects

In this subsection, the polarized corona emission has also a 2 per cent linear polarization but its initial Ψ is set to 0°, i.e. perpendicular to the projected symmetry axis of the disc. Results are plotted in Figs D1–D3.

Similarly to the previous case (2 per cent parallel), the spectroscopic channels are exactly the same as the unpolarized corona emission models. There is almost no differences in terms of polarization albeit the two remarks from Section 3.3, except that this time P is smaller than in the unpolarized cases at high energies and that the rotation of Ψ may vanish for some specific models. The first change is due to the orthogonality of the polarization vectors (from the primary source and from equatorial scattering), leading to a depolarization effect. The second is also linked with the transmission of photons with $\Psi = 0^\circ$ through the circumnuclear gaseous medium when the absorption column density is too low ($<10^{24}$ atm cm^{-2}), forcing the net polarization angle to the same value. Finally, we observe a slightly higher value of P in the soft energy band (when the Compton opacity is >1) for all the models with outflows. Since the polarization position angle due to polar scattering is the same as the initial polarization angle, P is strengthened by almost 2 per cent.

Ultimately, using a polarized primary in a type 2 AGN model without special or general relativity has minimal impact on to the resulting P and Ψ (if $P_{\rm init}$ is small). Depending on the configuration of the emission source, both polarization indicators can vary. If the initial polarization angle is parallel, the observed P will be slightly higher in the hard X-ray band, while if $\Psi_{\rm init}$ is perpendicular, it is the polarization of the soft X-ray band that will increase. However, in the soft band, scattering off the wind and torus completely dominates over the input polarization. If strong gravity effects are not important close to the central SMBH, it is unlikely that we will be able to retrieve the initial polarization of the continuum source when looking at type 2 AGN.

3.5 Results for a 2 per cent parallel polarized primary including strong gravity effects

For the last two subsections, we include both strong gravity effects and the polarization of the corona emission. Similarly to the previous case, we start with a 2 per cent parallel polarized primary and plot the results in Figs E1–E3.

The most striking result between models with and without strong gravity effects (and including a polarized corona emission) is visible in the energy-dependent polarization angle. Ψ smoothly rotates from large values to small angles at high energies, where photons can cross the equatorial region. The inclusion of a polarized corona emission drastically alters the value of Ψ for the models with a polar wind, while it has only a modest influence on the 'bare' AGN model. In particular, the rotation of the polarization angle is postponed to higher energies and the polarization degree observed at infinity is stronger than in the unpolarized primary case. Relativistic signatures can be seen in the polarimetric signal of photons with energy superior to the energy of Ψ transition, except in the case of a torus with hydrogen column density $\geq 10^{25}$ atm cm^{-2}. Photoelectric absorption is too strong for the remaining photons that scattered along equatorial plane to impose their polarization state over photons that have scattered off the winds or off the torus. An AGN dominated by highly ionized winds will also tend to smooth out the scattering-induced changes, revealing with higher precision the strong gravity effects.

3.6 Results for a 2 per cent perpendicular polarized primary including strong gravity effects

We find similar conclusions in the case of a 2 per cent perpendicular polarized corona emission including strong gravity effects, see Figs F1–F3. Most of the differences are related to the energy-dependent polarization angle that is quite distinct between the two initial polarization states. A primary emission with parallel polarization will create larger Ψ rotations than a corona emission with perpendicular polarization, allowing for a clear distinction between the two models. The degree of polarization follows the levels dictated by the source, with the exception of the high, scattering-induced polarization in the very soft band, where polar scattering dominates. Similarly to Section 3.4, P is higher in that energy band due to the similarity of the polarization angles between the source and the polar scattering mechanism.

Our principal conclusions can be summarized in Fig. 5. We plotted the results of a model with a Compton-thin absorbing polar outflow plus a circumnuclear molecular torus with $n_{\rm H_{torus}} = 10^{24}$ atm cm^{-2}. We included the results of a model where strong gravity effects are off, and results for a model where relativity is accounted for. We overplotted the outcomes for different models investigated in this paper, including perpendicularly polarized or unpolarized power laws, leading to a total four models. We leave aside the spectroscopic and polarization spectra of a model with parallel input polarization for clarity purposes, as the conclusions are very similar to the conclusions for the perpendicular polarization case.

All the models give very similar results in terms of spectroscopy, particularly below 10 keV. At higher energies, strong gravity effects tend to suppress the flux from the Compton hump with respect to the models with Newtonian physics. This is a behaviour expected from observations and simulations, see e.g. Risaliti et al. (2013) for an application to the galaxy NGC 1365, but it remains difficult to properly estimate all the model constituents to reproduce observations. A more secure option is to rely on X-ray polarimetry, as it can be seen in the third and fourth panels of Fig. 5. A model without a polarized corona emission, no strong gravity effects, will present a large degree of polarization in the soft X-ray band if polar scattering takes place but its P will be among the smallest at high energies. A rotation of 90° is expected between the two bands, with the polarization angle being either 0° or 90°. Including a polarized primary will only result in increasing P at high energies, making any distinction between the two models difficult, but allowing for an easier detection. A soon as the strong gravity effects are included, the polarization degree changes in the hard X-ray band and follows the polarization of the corona emission if photons are sufficiently energetic to pass through the circumnuclear gas without being absorbed. The polarization position angle keeps a trace of its initial polarization, showing smooth variations of Ψ with energy. Those variations strongly depend on the polarization of the primary emission, but they never rotate by 90° such as in the Newtonian case.

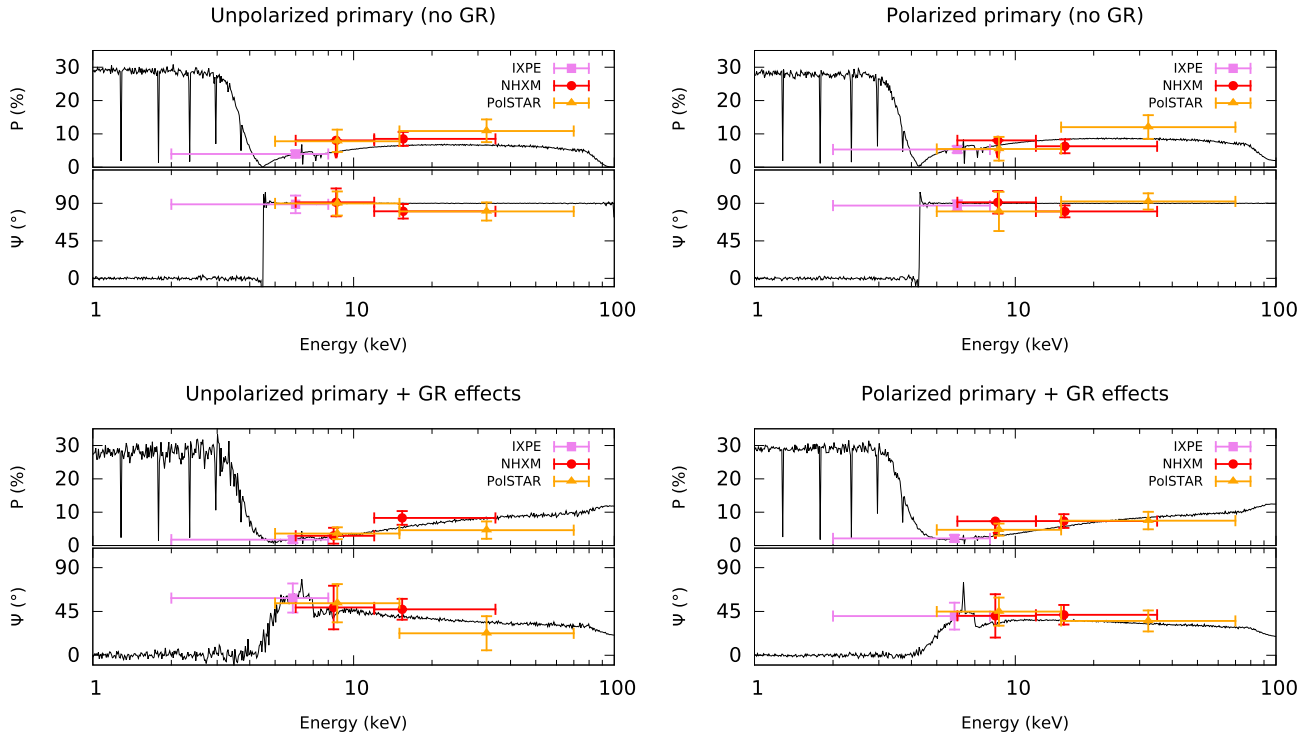

Figure 6. Simulated polarimetric observation for a generic Seyfert-2 galaxy. We used the energy spectrum and the polarization degrees and angles from the simulations presented in Fig. 5. The four spectra show the polarization for different parametrizations of the central source (top-left: unpolarized power law without general relativity; bottom-left: unpolarized power law with general relativity; top-right: perpendicularly polarized corona emission without general relativity; bottom-right: perpendicularly polarized corona emission with general relativity). The violet squares correspond to a 20 Ms observation with *IXPE*, the red circles correspond to a 2 Ms observation with *NHXM* and the orange triangles show a simulated 20 Ms observation with *PolSTAR*.

4 DETECTABILITY

We saw that including an initial polarization and strong gravity effects can have major repercussions on to the polarimetric signal from type 2 AGN. From our simulation, it is clear that even at edge-on inclinations it might be possible to detect special and general relativity effects imprinted in the X-ray polarimetric spectra if the amount of obscuring hydrogen column density along the observer's line-of-sight is not equal or larger than 10^{25} atm cm^{-2}. Hence, in the following section, we will investigate the detectability of a typical type 2 AGN such as presented in Figs 1 and 5, using three different space missions. To illustrate this example, we set the X-ray flux of the model to equal the broad-band X-ray flux of NGC 1068 (Matt et al. 2004; Pounds & Vaughan 2006; Cardamone, Moran & Kay 2007), an archetypal Seyfert-2 galaxy. The Galactic column density towards this AGN was estimated to be close to 2.99×10^{20} cm^{-2} (Murphy et al. 1996), and we accounted for this value in our estimations of the observed X-ray polarization.

4.1 With the *Imaging X-ray Polarimetry Explorer*

Our first prediction concerns the *Imaging X-ray Polarimetry Explorer* (*IXPE*), a NASA-SMEX mission that was selected on 2017 January the 3 for launch in late 2020. The *IXPE* spacecraft will study black holes and other high energy astronomical phenomena thanks to its three telescopes dedicated to X-ray polarimetry (Weisskopf et al. 2016). The energy range of sensitivity, between 2 and 8 keV, will allow to observe representative objects belonging to basically all the classes of high-energy sources. For several extended sources, *IXPE* will perform imaging polarimetry for the first time. The capability to measure also the time of arrival and the energy of the absorbed photons will allow to perform time and spectrally resolved measurements.

Detectability of the effects presented in the previous sections was evaluated by means of Monte Carlo simulations, performed with the same code used in Dovčiak et al. (2011) or in Taverna et al. (2014). The source spectra and the instrument effective area are used to compute the counting rate on the instrument, whereas the source polarization and the amplitude of the instrumental response to polarization, expressed through the modulation factor, are used to derive the amplitude of the expected signal. The code eventually returns a modulation curve which is representative of the output of the real instrument; this is processed like real data and an estimate of the measured polarization, together with its error, is obtained.

We present in Fig. 6 the detectability of the *IXPE* mission. The minimum detectable polarization (MDP), which is the degree of polarization corresponding to the amplitude of modulation that has only a 1 per cent probability of being detected by chance, is about 3 per cent in this case. Errors are at 1σ confidence level only if we want to measure just one parameter (the degree or the angle of polarization, but not both); see Strohmayer & Kallman (2013). If we aim to measure both polarization parameters, the 1σ errors are about 50 per cent larger. To achieve a detection of the polarimetric signal in the 2–8 keV, we estimate that a 20 Ms observation with *IXPE* is necessary. Despite a large polarization degree in the soft X-ray band, the relative dimness of type 2 AGN compared to type-1 objects (unobscured by the equatorial torus) drives longer observational requirements. For this reason, we integrated the X-ray polarization over the whole energy band of *IXPE* in order to minimize the observational time, resulting in only one measurement.

Since the polarization of our models shows energy-dependent polarization properties, it would be beneficial to have a complementary observation in a harder X-ray band. This could be achieved thanks to the following polarimetric mission concepts.

4.2 With the *New Hard X-ray Mission*

The *New Hard X-ray Mission* (*NHXM*) was a concept mission based on new technologies in mirror and detector manufacturing, aiming to achieve imaging X-ray spectroscopy and polarimetry in a broad-band energy range (Tagliaferri et al. 2012). A set of three X-ray optics based on multilayer technology was coupled with focal plane detectors to achieve imaging and spectroscopy between 0.5 and 80 keV; a fourth optics was dedicated to imaging X-ray polarimetry with the alternate use of two gas pixel detectors optimized in the 2–10 and 6–35 keV energy range. The latter, called medium energy polarimetry (MEP), is particularly indicated to study the effects presented above, because the sensitivity is in the energy range where the polarization signal is higher. To evaluate the detectability with *NHXM*, we used the same approach followed for *IXPE*.

Thanks to its MEP, the *NHXM* mission would have been able to measure the energy-dependent X-ray polarization of Seyfert-2 galaxies. The MDP in the soft band is of the order of 8 per cent, while it is about 6 per cent in the higher energy band. The amount of time necessary to achieve those measurement would have been 10 times shorter than for the *IXPE* mission, about 2 Ms here (see Fig. 6). The acquisition of two data point would have been sufficient to distinguish between the models with and without strong gravity effects. However, a longer exposure time would have been necessary to distinguish between a polarized and an unpolarized primary emission.

4.3 With the *Polarization Spectroscopic Telescope Array*

The *Polarization Spectroscopic Telescope Array* (*PolSTAR*) is a mission designed to measure 3–50 keV polarization of compact objects with a scattering polarimeter, which was proposed in response to NASA's 2014 SMEX announcement of opportunity (Krawczynski et al. 2011, 2016b). *PolSTAR* is built on technology developed for *NuSTAR*, namely its X-ray optics, extensible telescope boom, optical bench and CdZnTe detectors. In *PolSTAR*, the X-rays are focused on to a cylindrical LiH scattering element surrounded by 16 CZT detectors to measure the scattered X-rays. The technique makes use of the fact that photons scatter preferentially perpendicular to their polarization direction. *PolSTAR* has a relatively uniform modulation factor of $\mu \sim 0.5$ throughout its entire energy bandwidth. It achieves its maximum polarization sensitivity between 7 and 14 keV, with an MDP of 1 per cent for an 860 ks observation of a 20 mCrab source.

In order to simulate the response of *PolSTAR* for our AGN model, we normalized the absorbed model flux to the observed *ASCA* 2–8 keV flux of 5.19×10^{-12} erg cm^{-2} s^{-1}. We then numerically integrated the reduced Stokes parameters of the model, $\mathcal{Q}_r$ and $\mathcal{U}_r$, see Kislat et al. (2015), over the simulated energy bins (5–15 and 15–70 keV). Finally, we calculated the expected number of signal and background events, N_s and N_{BG}, in each bin. The observed polarization fraction and angle were then drawn from the distribution (Vinokur 1965; Weisskopf 2009; Krawczynski 2011):

$$P(p, \psi | p_0, \psi_0) = \frac{N_{obs}^2 \mu^2 p}{4\pi(N_{obs} + N_{BG})} \exp[A],$$

with

$$A = -\frac{N_{obs}^2 \mu^2}{4(N_{obs} + N_{BG})} \left(p_0^2 + p^2 - 2pp_0 \cos(2(\psi - \psi_0))\right),$$

where $p_0 = \sqrt{\mathcal{Q}_r + \mathcal{U}_r}$ and $\psi_0 = \frac{1}{2} \arctan \frac{\mathcal{U}_r}{\mathcal{Q}_r}$ are the true polarization fraction and angle, and N_{obs} is the simulated number of signal photons due to N_s. The expected number of background events, N_{BG}, is based on the observed *NuSTAR* background, scaled to account for the larger detector area.

To measure the soft and hard X-ray polarization of our model of type 2 AGN and distinguish between an unpolarized/polarized source dominated (or not) by strong gravity effects, about 20 Ms is required (see Fig. 6). This is 10 times higher than for the *NHXM* mission, but it is scaled with the physical size of the detectors (where *NHXM* was intended to be a medium-sized satellite). A broad-band X-ray polarimeter able to measure the polarization in the Compton hump gives a clear picture of the importance of strong gravity effects, with the polarization position angle showing a larger rotation between the soft and hard X-ray bins of *PolSTAR* with respect to the other two missions.

Ultimately, a measurement of the X-ray polarization of type 2 AGN is within the capabilities of the aforementioned three instruments but long observing times are required. This is due to the obscuration of the central source by the optically thick molecular gas around the equatorial plane. Despite the high degree of polarization expected in the soft X-ray band, the starvation of photons hampers an easy detection of the polarimetric signatures of obscured objects, and we showed here that at least a couple of megaseconds is required (with the exact amount of time needed being model dependent).

5 CONCLUSIONS

In this paper, we explored in great details the X-ray polarization emerging from complex type 2 AGN modelling. For the first time, we coupled the strong gravity effects near the horizon of the central SMBH to the distant scattering and absorbing media that shape the observed fluxes of Seyfert galaxies. To do so, we used the KY code that computes the parallel transport of polarization along the photon null geodesics close to a potential well and, from a certain radius where relativistic effects are no longer important, the radiative transfer code STOKES takes over to propagate radiation through the torus and polar winds. It results in the first coherent modelling of X-ray polarization from type 2 AGN. We explored a large variety of AGN structures, including or excluding winds (either ionized or filled with neutral, cold matter), and varying the hydrogen column density along the observer's line-of-sight intercepted by the puffed-up torus. The polarization state of the continuum source was investigated and we analysed how the initial polarization modify the final polarization observed at infinity.

We found that Seyfert-2s with clear electron scattering in their soft X-ray spectra (such as NGC 4945; see Madejski et al. 2000; Puccetti et al. 2014) are excellent potential targets for a future polarimetric detection as, regardless of the ionization stage of the wind, we expect a large polarization degree at soft X-ray energies. On the other hand, Compton-thick, windless AGN such as the equivalent of bare type-1 AGN (Patrick et al. 2011) might be more problematic to observe due to the strong absorption of photons below 10 keV. If strong gravity effects are not dominant close to the central engine, then the polarization position angle can take only two values (0° and 90°). However, when special and general relativity are accounted, then the polarization position angle can rotate smoothly between the

soft and hard X-ray bands. This is an important result as, similarly to what we foresee for type-1s, looking at the polarization angle of type 2s will definitively tell us if strong gravity effects are important close to the central compact source.

If special and general relativity are not shaping the X-ray spectrum of AGN close to the potential well, modifying the initial polarization of the continuum will not affect the final polarization degree. Scattering off the winds and torus completely dominates the input polarization and it is impossible to retrieve the initial polarization of the continuum source when looking at type 2s. However, by looking at the energy at which the polarization position angle rotates from 0° to 90°, it becomes feasible to derive the hydrogen column density along the line-of-sight (with a small degeneracy on the observer's inclination).

Adding strong gravity effects completely changes the picture. First the polarization angle becomes energy dependent and differs between a Schwarzschild and a Kerr black hole. In the soft X-ray band, photoionization dominates and most of the information about the spin of the central source is lost due to the overwhelming importance of polar scattering in the wind. At higher energies (or for Compton-thin type 2s), photons can travel through the equatorial gaseous medium and it becomes feasible to observe the energy-dependent variation of the polarization angle, together with a different polarization degree than what is expected from the purely Newtonian case. Unfortunately, a polarized or an unpolarized primary radiation has almost no effect on to the final polarization spectrum of a type 2 AGN, independently of the inclusion of strong gravity effects or not. This is a very different conclusion from what we expect for type-1s.

We have shown that the future generation of X-ray polarimeters will be able to measure the degree and angle of polarization for type 2 objects, albeit long integration times (over a megasecond, even for bright type 2s). With the development of photoelectric and scattering polarimeters, and the ever-improving resolution and sensitivity of modern satellites, it will be soon possible to unveil the physical effects and the organization of matter even in the most obscured astronomical sources thanks to X-ray polarimetry.

ACKNOWLEDGEMENTS

The authors are grateful to Ski Antonucci for his remarkable suggestions about the X-ray spectra of type 2 AGN, and to René W. Goosmann for his help with the code and the English grammar. FM would like to thank the meso-center of Strasbourg, partner of the CPER 2015–2020 project 'Alsacalcul', for allocating us the time to run our simulations. FFK and HSK acknowledge funding from NASA through Grants NNX10AJ56G, NNX12AD51G and NNX14AD19G.

REFERENCES

Antonucci R., 1993, ARA&A, 31, 473
Beilicke M. et al., 2012, in Aharonian F. A., Hofmann W., Rieger F. M., eds, AIP Conf. Proc. Vol. 1505, High Energy Gamma-Ray Astronomy: 5th International Meeting on High Energy Gamma-Ray Astronomy. Am. Inst. Phys., New York, p. 805
Beilicke M. et al., 2014, J. Astron. Instrum., 3, 1440008
Bellazzini R. et al., 2006, Nucl. Instrum. Methods Phys. Res. A, 566, 552
Bellazzini R. et al., 2007, Nucl. Instrum. Methods Phys. Res. A, 579, 853
Buchner J. et al., 2015, ApJ, 802, 89
Cardamone C. N., Moran E. C., Kay L. E., 2007, AJ, 134, 1263
Chandrasekhar S., 1960, Radiative Transfer. Dover Press, New York
Chauvin M. et al., 2016, MNRAS, 456, L84
Connors P. A., Stark R. F., 1977, Nature, 269, 128
Connors P. A., Stark R. F., Piran T., 1980, ApJ, 235, 224
Costa E., Soffitta P., Bellazzini R., Brez A., Lumb N., Spandre G., 2001, Nature, 411, 662
Dovčiak M., Bianchi S., Guainazzi M., Karas V., Matt G., 2004, MNRAS, 350, 745
Dovčiak M., Muleri F., Goosmann R. W., Karas V., Matt G., 2008, MNRAS, 391, 32
Dovčiak M., Muleri F., Goosmann R. W., Karas V., Matt G., 2011, ApJ, 731, 75
Dumont A.-M., Abrassart A., Collin S., 2000, A&A, 357, 823
Fabian A. C., 2012, ARA&A, 50, 455
Fanidakis N., Baugh C. M., Benson A. J., Bower R. G., Cole S., Done C., Frenk C. S., 2011, MNRAS, 410, 53
Ferrarese L., Merritt D., 2000, ApJ, 539, L9
Fritz J., Franceschini A., Hatziminaoglou E., 2006, MNRAS, 366, 767
Gebhardt K. et al., 2000, ApJ, 539, L13
Giacconi R., Gursky H., Paolini F. R., Rossi B. B., 1962, Phys. Rev. Lett., 9, 439
Giacconi R., Gursky H., Waters J. R., 1964, Nature, 204, 981
Goosmann R. W., Gaskell C. M., 2007, A&A, 465, 129
Haardt F., Maraschi L., 1991, ApJ, 380, L51
Haardt F., Maraschi L., 1993, ApJ, 413, 507
Halpern J. P., 1984, ApJ, 281, 90
Hoormann J. K., Beheshtipour B., Krawczynski H., 2016, Phys. Rev. D., 93, 044020
Inoue H., Matsumoto C., 2003, PASJ, 55, 625
Kamae T. et al., 2008, Astropart. Phys., 30, 72
Kauffmann G., Haehnelt M., 2000, MNRAS, 311, 576
Kinkhabwala A. et al., 2002, ApJ, 575, 732
Kislat F., Clark B., Beilicke M., Krawczynski H., 2015, Astropart. Phys., 68, 45
Krawczynski H., 2011, Astropart. Phys., 34, 784
Krawczynski H., Garson A., Guo Q., Baring M. G., Ghosh P., Beilicke M., Lee K., 2011, Astropart. Phys., 34, 550
Krawczynski H., Kislat F., Stuchlik D., Okajima T., de Geronimo G., 2016a, Am. Astron. Soc., HEAD Meeting, 15, 116.20
Krawczynski H. S. et al., 2016b, Astropart. Phys., 75, 8
McLure R. J., Dunlop J. S., Kukula M. J., 2000, MNRAS, 318, 693
McNamara A. L., Kuncic Z., Wu K., 2009, MNRAS, 395, 1507
Madejski G., Życki P., Done C., Valinia A., Blanco P., Rothschild R., Turek B., 2000, ApJ, 535, L87
Magorrian J. et al., 1998, AJ, 115, 2285
Marin F., 2014, MNRAS, 441, 551
Marin F., 2016, MNRAS, 460, 3679
Marin F., Goosmann R. W., Dovčiak M., Muleri F., Porquet D., Grosso N., Karas V., Matt G., 2012a, MNRAS, 426, L101
Marin F., Goosmann R. W., Gaskell C. M., Porquet D., Dovčiak M., 2012b, A&A, 548, A121
Marin F., Porquet D., Goosmann R. W., Dovčiak M., Muleri F., Grosso N., Karas V., 2013, MNRAS, 436, 1615
Marin F., Goosmann R. W., Gaskell C. M., 2015, A&A, 577, A66
Marin F., Goosmann R. W., Petrucci P.-O., 2016, A&A, 591, A23
Marinucci A. et al., 2016, MNRAS, 456, L94
Matt G., Costa E., Perola G. C., Piro L., 1989, in Hunt J., Battrick B., eds, Proc. 23rd ESLAB Symp., Two Topics in X-Ray Astronomy. ESA SP-296, ESA, Noordwijk, p. 991
Matt G., Fabian A. C., Ross R. R., 1993, MNRAS, 264, 839
Matt G., Bianchi S., Guainazzi M., Molendi S., 2004, A&A, 414, 155
Meier D. L., 2002, New Astron. Rev., 46, 247
Miller L., Turner T. J., 2013, ApJ, 773, L5
Miller L., Turner T. J., Reeves J. N., 2008, A&A, 483, 437
Miller L., Turner T. J., Reeves J. N., 2009, MNRAS, 399, L69
Murphy E. M., Lockman F. J., Laor A., Elvis M., 1996, ApJS, 105, 369
Nandra K., Pounds K. A., 1994, MNRAS, 268, 405
Nandra K., George I. M., Mushotzky R. F., Turner T. J., Yaqoob T., 1997, ApJ, 477, 602
Nandra K. et al., 2007, ApJ, 660, L11

Novick R., Weisskopf M. C., Berthelsdorf R., Linke R., Wolff R. S., 1972, ApJ, 174, L1
Page K. L., Reeves J. N., O'Brien P. T., Turner M. J. L., 2005, MNRAS, 364, 195
Patrick A. R., Reeves J. N., Porquet D., Markowitz A. G., Lobban A. P., Terashima Y., 2011, MNRAS, 411, 2353
Pearce M., 2012, in Simone G. et al., eds, Proceedings of the 13th ICATPP Conference. Astroparticle, Particle, Space Physics and Detectors For Physics Applications. World Scientific Publishing Co. Pte. Ltd., p. 151
Pineault S., 1977, MNRAS, 179, 691
Porquet D., Dubau J., 2000, A&AS, 143, 495
Pounds K., Vaughan S., 2006, MNRAS, 368, 707
Pringle J. E., Rees M. J., 1972, A&A, 21, 1
Puccetti S. et al., 2014, ApJ, 793, 26
Risaliti G., Elvis M., Fabbiano G., Baldi A., Zezas A., 2005, ApJ, 623, L93
Risaliti G. et al., 2013, Nature, 494, 449
Schawinski K. et al., 2009, ApJ, 690, 1672
Schawinski K., Koss M., Berney S., Sartori L. F., 2015, MNRAS, 451, 2517
Schnittman J. D., Krolik J. H., 2009, ApJ, 701, 1175
Schnittman J. D., Krolik J. H., 2010, ApJ, 712, 908
Schnittman J. D., Krolik J. H., 2013, ApJ, 777, 11
Shakura N. I., Sunyaev R. A., 1973, A&A, 24, 337
Siebenmorgen R., Heymann F., Efstathiou A., 2015, A&A, 583, A120
Springel V. et al., 2005, Nature, 435, 629
Streblyanska A., Hasinger G., Finoguenov A., Barcons X., Mateos S., Fabian A. C., 2005, A&A, 432, 395
Strohmayer T. E., Kallman T. R., 2013, ApJ, 773, 103
Suganuma M. et al., 2006, ApJ, 639, 46
Tagliaferri G., Hornstrup A., Huovelin J., Reglero V., Romaine S., Rozanska A., Santangelo A., Stewart G., 2012, Exp. Astron., 34, 463
Taverna R., Muleri F., Turolla R., Soffitta P., Fabiani S., Nobili L., 2014, MNRAS, 438, 1686
Tombesi F., Cappi M., Reeves J. N., Palumbo G. G. C., Yaqoob T., Braito V., Dadina M., 2010, A&A, 521, A57
Tombesi F., Cappi M., Reeves J. N., Nemmen R. S., Braito V., Gaspari M., Reynolds C. S., 2013, MNRAS, 430, 1102
Ueda Y., 2015, Proc. Jpn. Acad. Ser. B, 91, 175
Urry C. M., Padovani P., 1995, PASP, 107, 803
Vinokur M., 1965, Ann. d'Astrophys., 28, 412
Weisskopf M. C., 2010, in Bellazzini R., Costa E., Matt G., Tagliaferri G., eds, X-ray Polarimetry: A New Window in Astrophysics. Cambridge Univ. Press, Cambridge, p. 1
Weisskopf M. C., Cohen G. G., Kestenbaum H. L., Long K. S., Novick R., Wolff R. S., 1976, ApJ, 208, L125
Weisskopf M. C., Silver E. H., Kestenbaum H. L., Long K. S., Novick R., 1978, ApJ, 220, L117
Weisskopf M. C., Elsner R. F., Hanna D., Kaspi V. M., O'Dell S. L., Pavlov G. G., Ramsey B. D., 2009, Astrophys. Space Sci. Libr., 357, 589
Weisskopf M. C. et al., 2016, Proc. SPIE, 9905, 990517
Winter L. M., Mushotzky R. F., Reynolds C. S., Tueller J., 2009, ApJ, 690, 1322
Woo J.-H., Urry C. M., 2002, ApJ, 581, L5
Yaqoob T., Padmanabhan U., 2004, ApJ, 604, 63

APPENDIX A

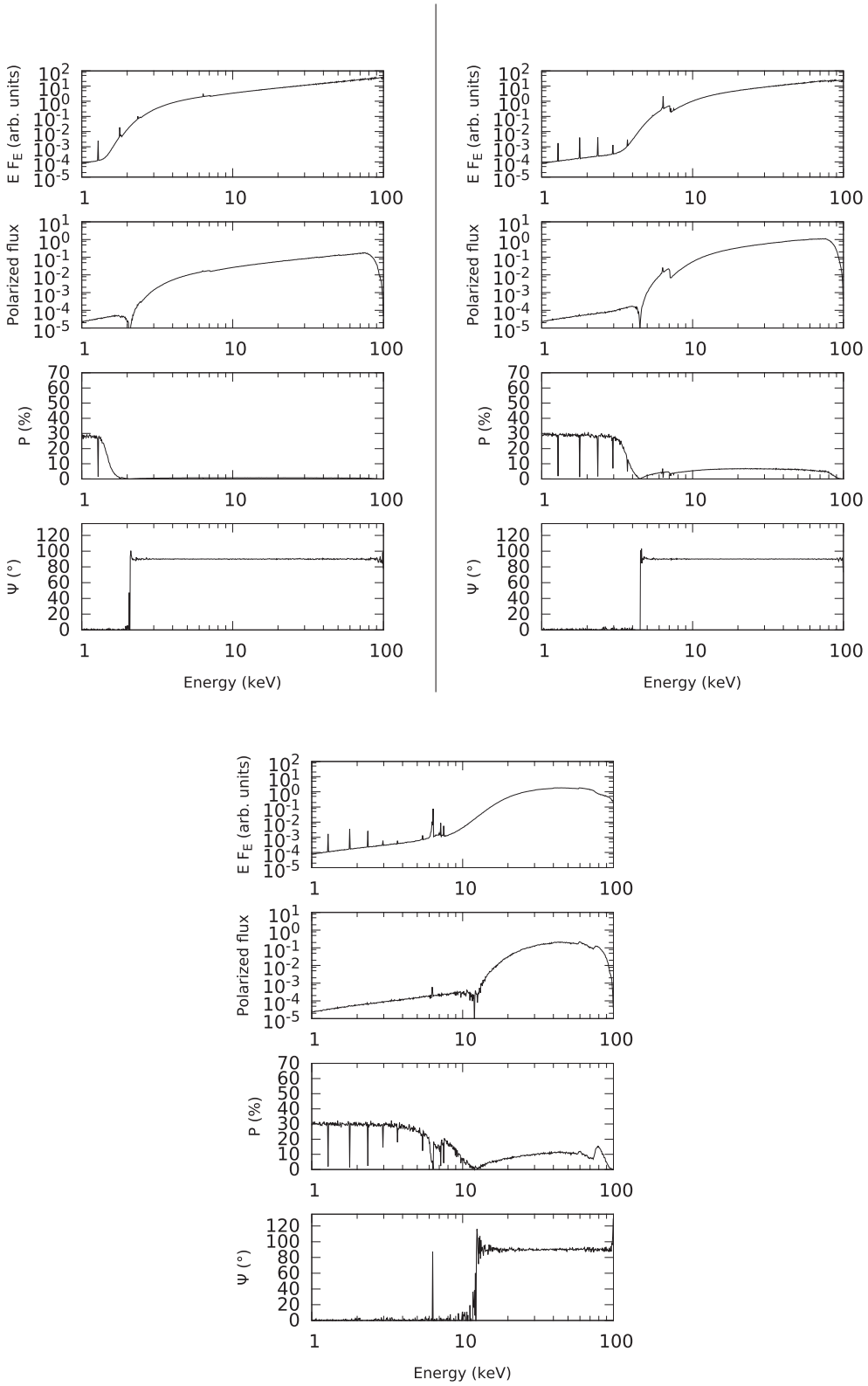

Figure A1. X-ray flux (F_E is energy flux at energy E), polarized flux, polarization degree and polarization position angle for a type 2 AGN with Compton-thin absorbing polar winds ($n_{\rm H_{wind}} = 10^{21}$ atm cm^{-2}). Top-left: $n_{\rm H_{torus}} = 10^{23}$ atm cm^{-2}; top-right: 10^{24} atm cm^{-2}; bottom: 10^{25} atm cm^{-2}. See text for additional details about the model components. The input spectrum is unpolarized. Strong gravity effects are not included.

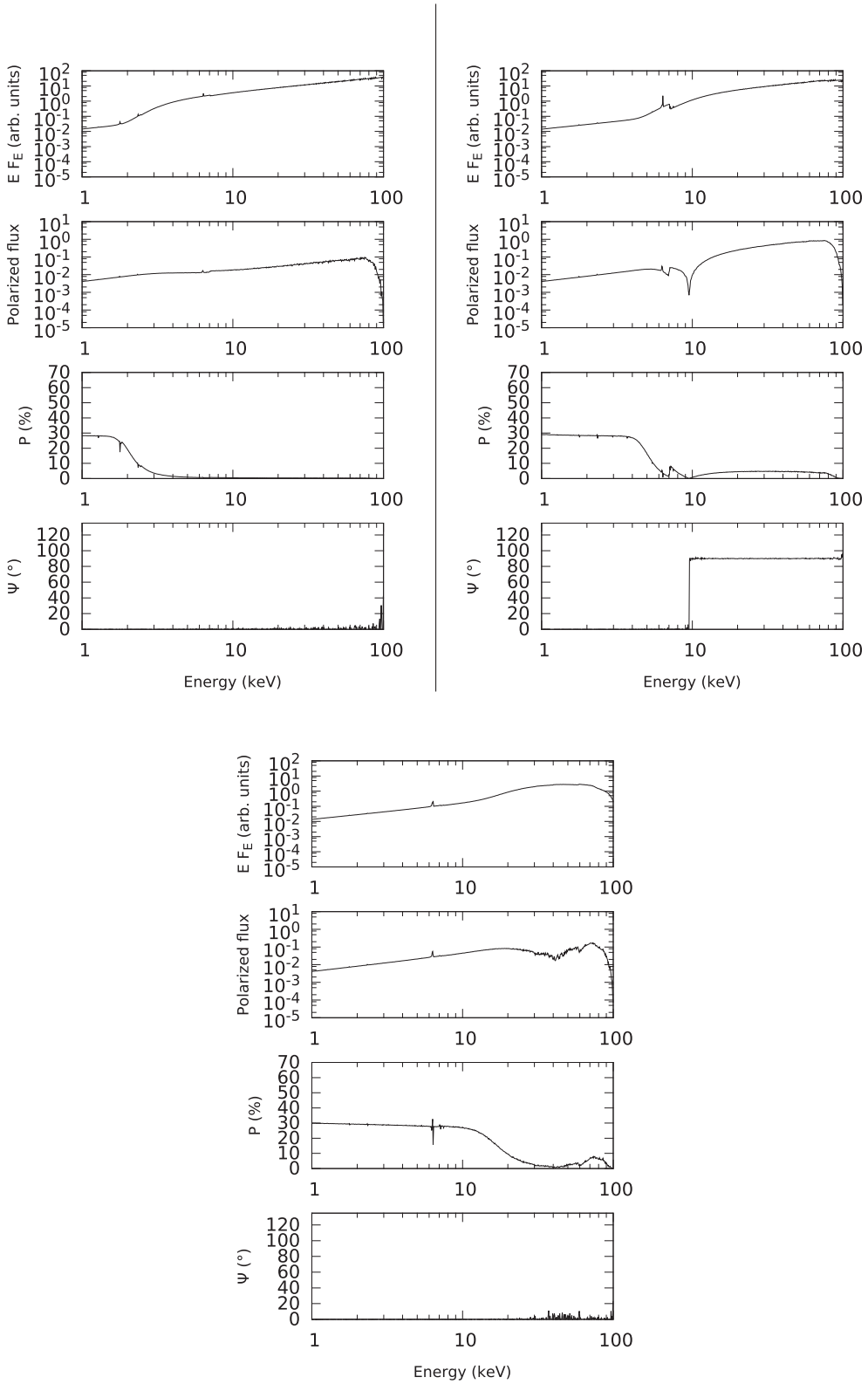

Figure A2. X-ray flux (F_E is energy flux at energy E), polarized flux, polarization degree and polarization position angle for a type 2 AGN with fully ionized polar winds. Top-left: $n_{\mathrm{H_{torus}}} = 10^{23}$ atm cm^{-2}; top-right: 10^{24} atm cm^{-2}; bottom: 10^{25} atm cm^{-2}. See text for additional details about the model components. The input spectrum is unpolarized. Strong gravity effects are not included.

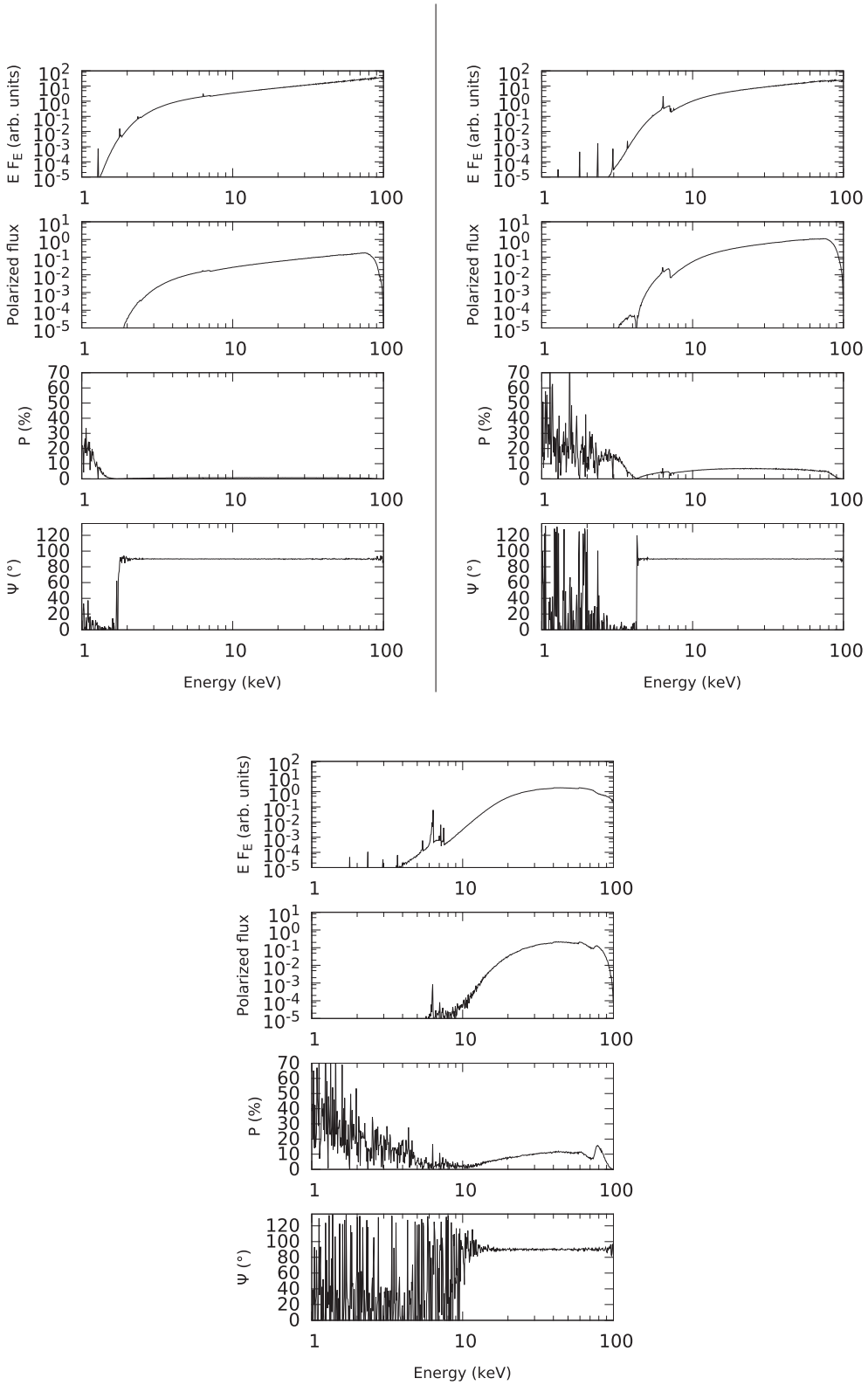

Figure A3. X-ray flux (F_E is energy flux at energy E), polarized flux, polarization degree and polarization position angle for a type 2 AGN without polar winds. Top-left: $n_{\mathrm{H_{torus}}} = 10^{23}$ atm cm^{-2}; top-right: 10^{24} atm cm^{-2}; bottom: 10^{25} atm cm^{-2}. See text for additional details about the model components. The input spectrum is unpolarized. Strong gravity effects are not included.

APPENDIX B

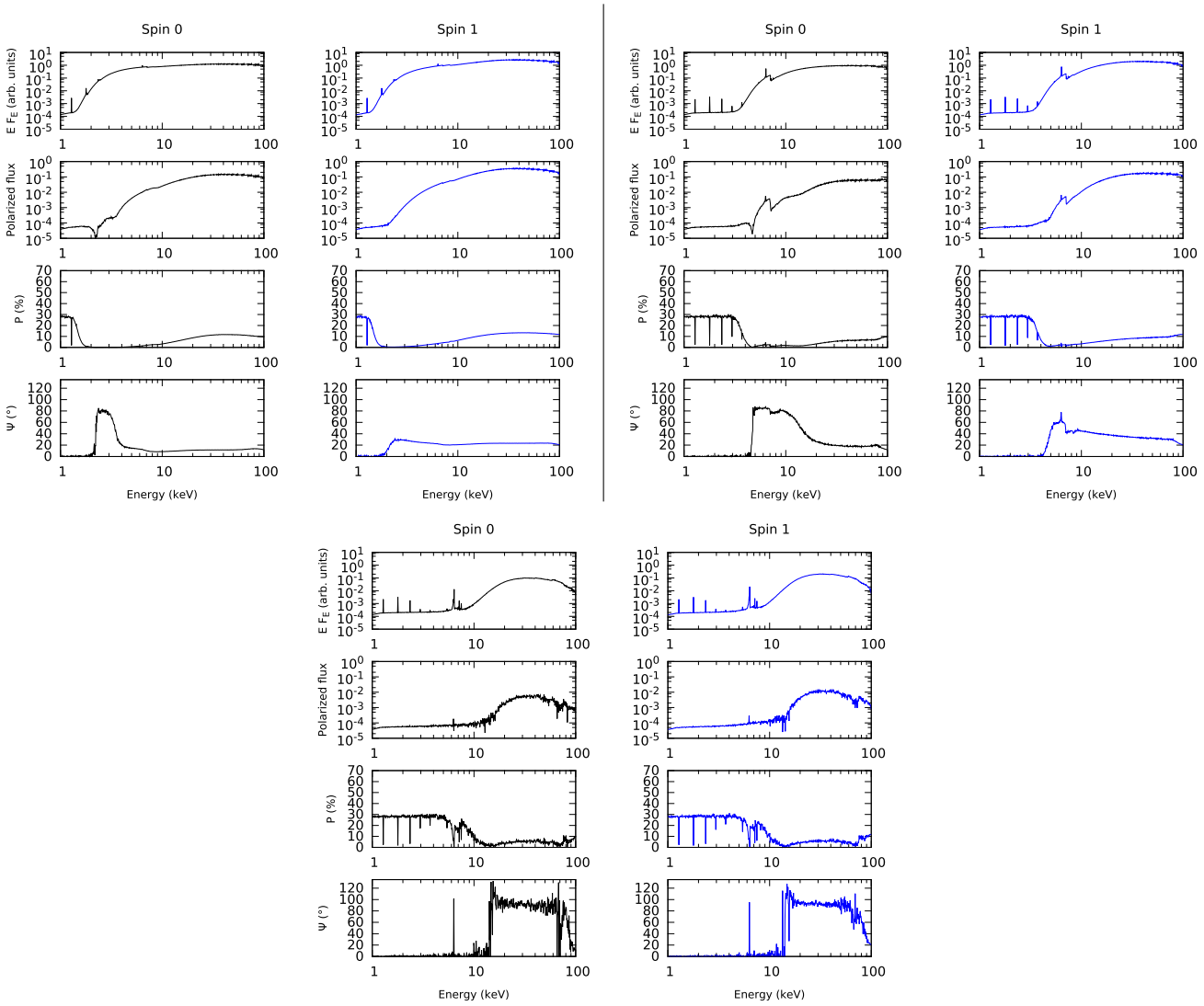

Figure B1. X-ray flux (F_E is energy flux at energy E), polarized flux, polarization degree and polarization position angle for a type 2 AGN with Compton-thin absorbing polar winds ($n_{\rm H_{wind}} = 10^{21}$ atm cm^{-2}). Top-left: $n_{\rm H_{torus}} = 10^{23}$ atm cm^{-2}; top-right: 10^{24} atm cm^{-2}; bottom: 10^{25} atm cm^{-2}. See text for additional details about the model components. The input spectrum is unpolarized. Strong gravity effects are included.

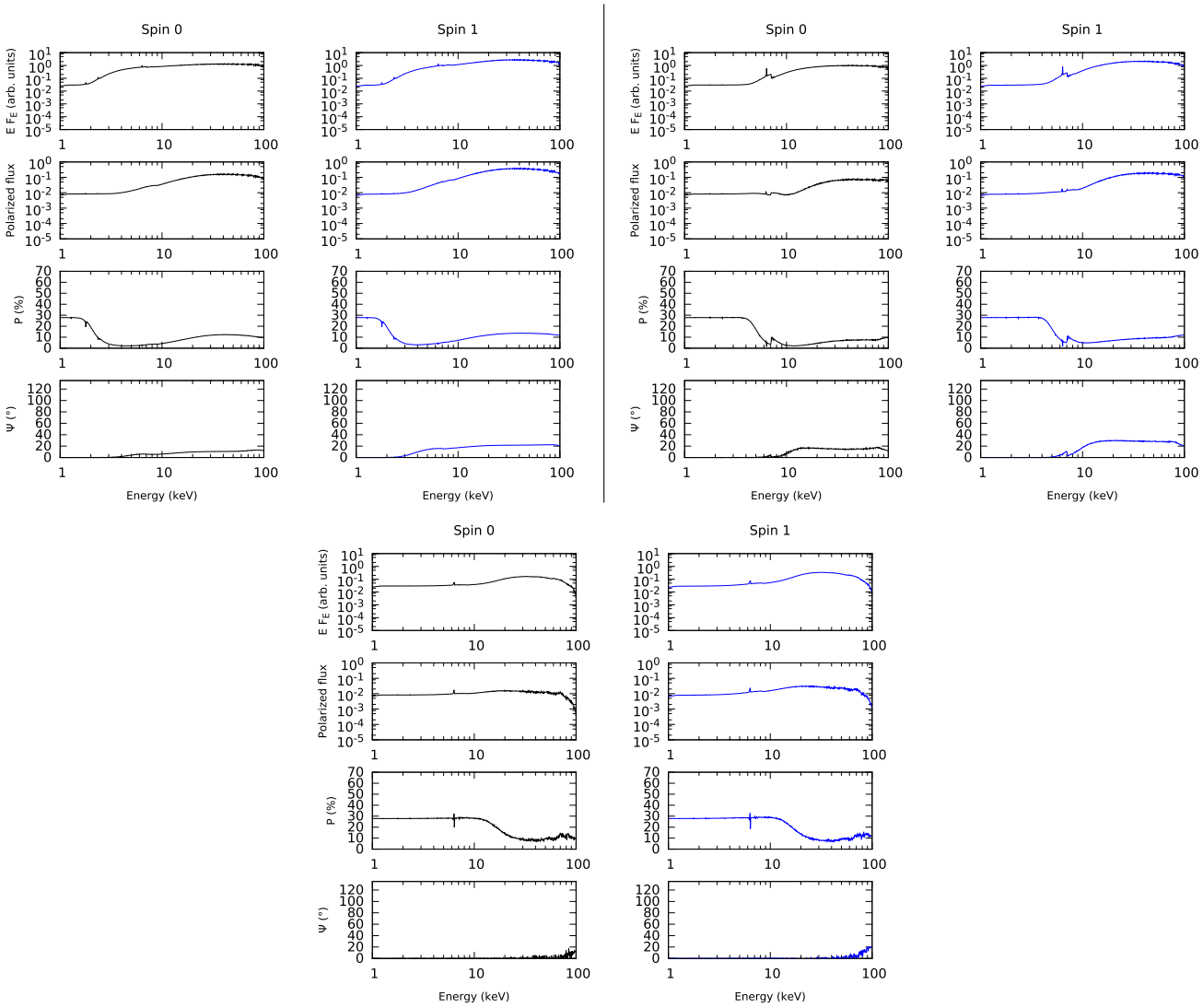

Figure B2. X-ray flux (F_E is energy flux at energy E), polarized flux, polarization degree and polarization position angle for a type 2 AGN with fully ionized polar winds. Top-left: $n_{\rm H_{torus}} = 10^{23}$ atm cm^{-2}; top-right: 10^{24} atm cm^{-2}; bottom: 10^{25} atm cm^{-2}. See text for additional details about the model components. The input spectrum is unpolarized. Strong gravity effects are included.

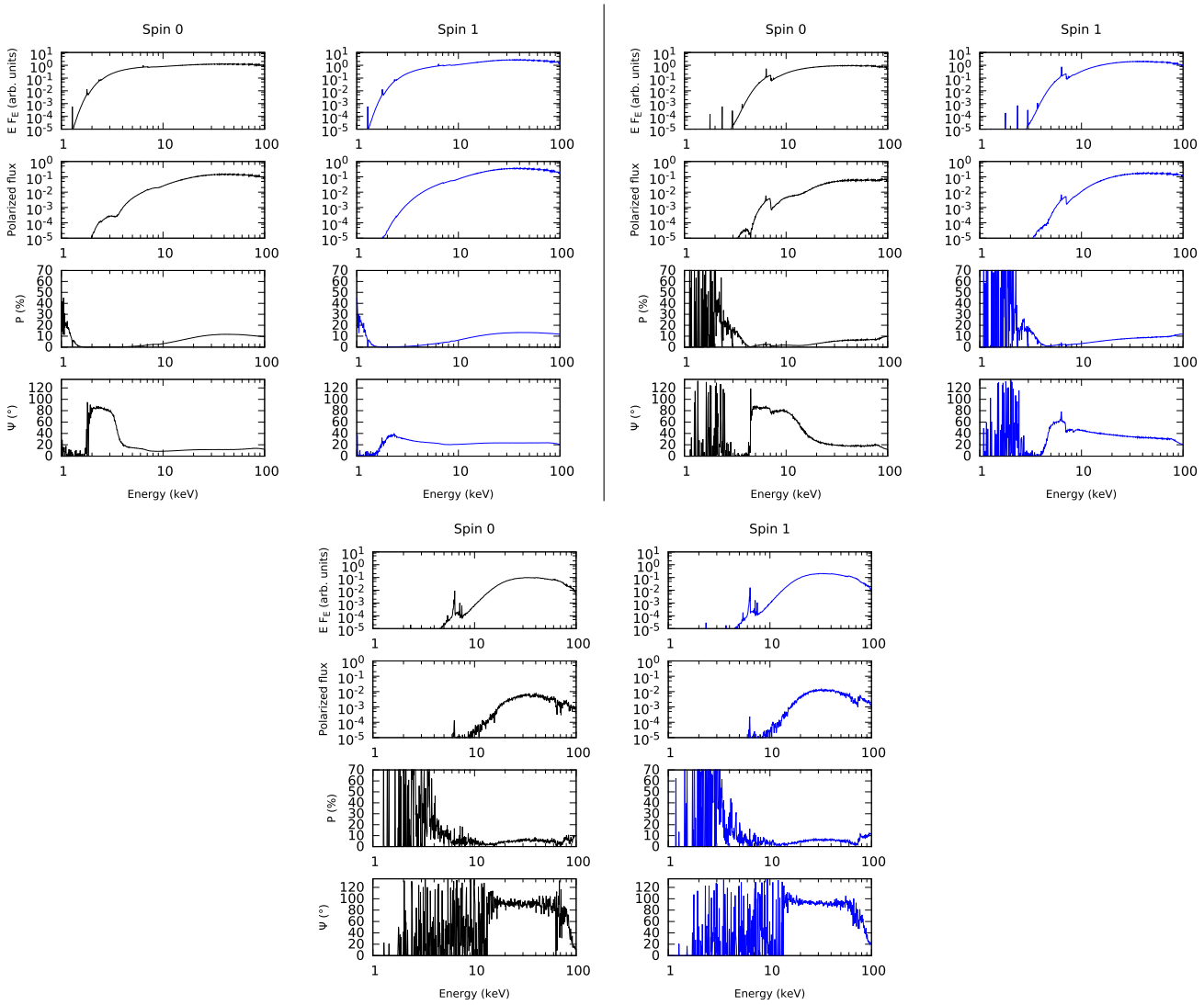

Figure B3. X-ray flux (F_E is energy flux at energy E), polarized flux, polarization degree and polarization position angle for a type 2 AGN without polar winds. Top-left: $n_{\rm H_{torus}} = 10^{23}$ atm cm^{-2}; top-right: 10^{24} atm cm^{-2}; bottom: 10^{25} atm cm^{-2}. See text for additional details about the model components. The input spectrum is unpolarized. Strong gravity effects are included.

APPENDIX C

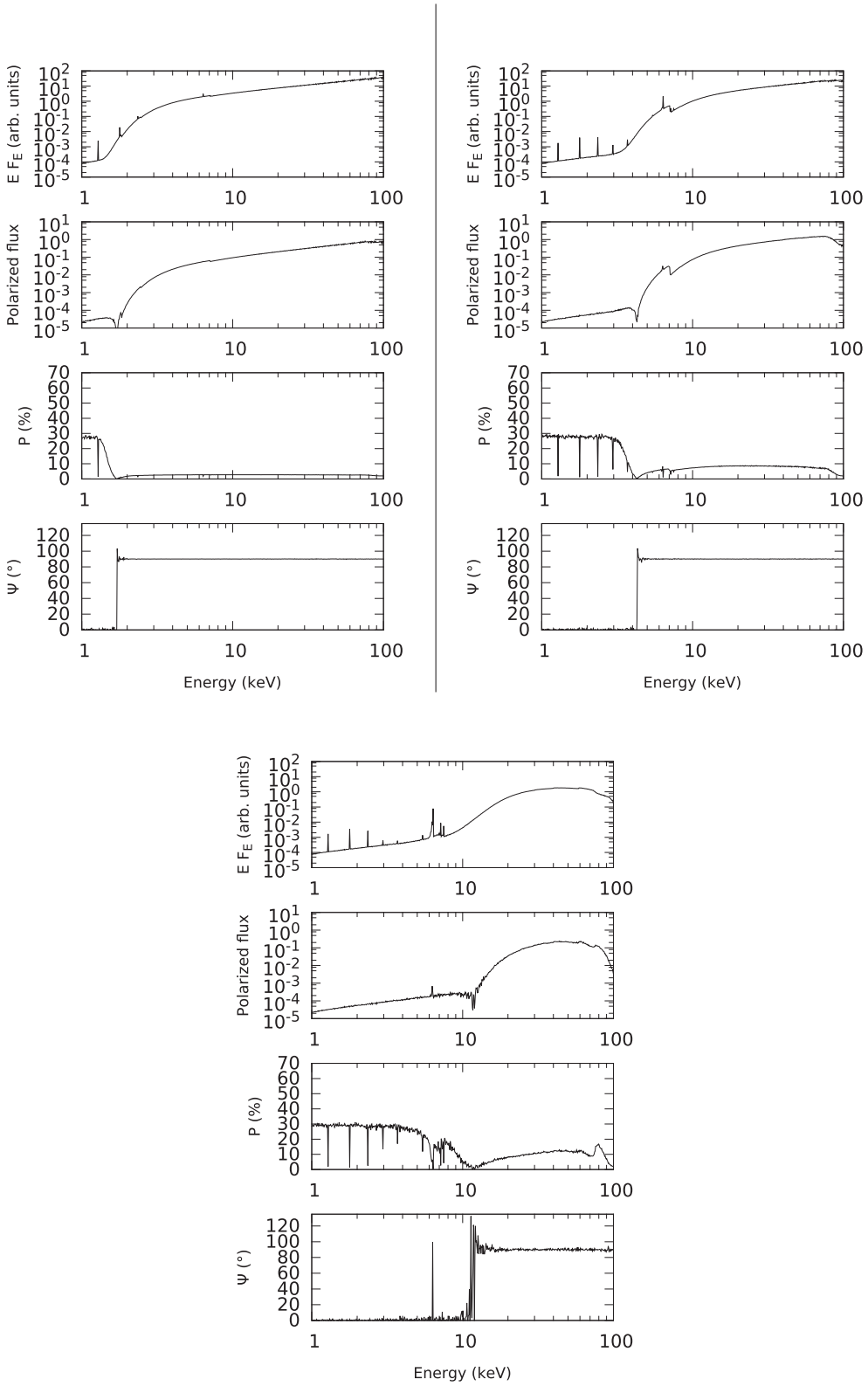

Figure C1. X-ray flux (F_E is energy flux at energy E), polarized flux, polarization degree and polarization position angle for a type 2 AGN with Compton-thin absorbing polar winds ($n_{\rm H_{wind}} = 10^{21}$ atm cm^{-2}). Top-left: $n_{\rm H_{torus}} = 10^{23}$ atm cm^{-2}; top-right: 10^{24} atm cm^{-2}; bottom: 10^{25} atm cm^{-2}. See text for additional details about the model components. The input spectrum is polarized (2 per cent parallel polarization). Strong gravity effects are not included.

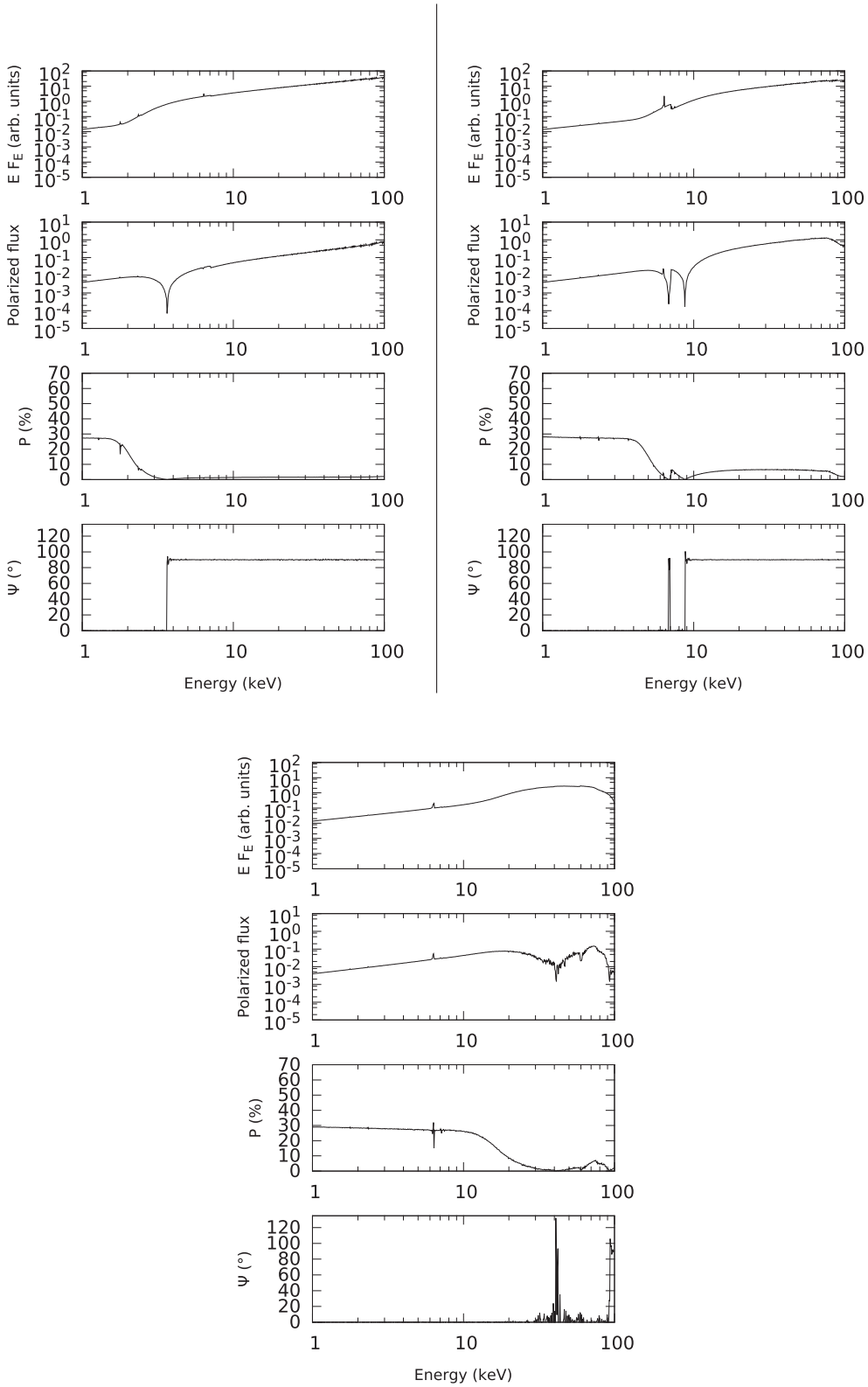

Figure C2. X-ray flux (F_E is energy flux at energy E), polarized flux, polarization degree and polarization position angle for a type 2 AGN with fully ionized polar winds. Top-left: $n_{\mathrm{H_{torus}}} = 10^{23}$ atm cm^{-2}; top-right: 10^{24} atm cm^{-2}; bottom: 10^{25} atm cm^{-2}. See text for additional details about the model components. The input spectrum is polarized (2 per cent parallel polarization). Strong gravity effects are not included.

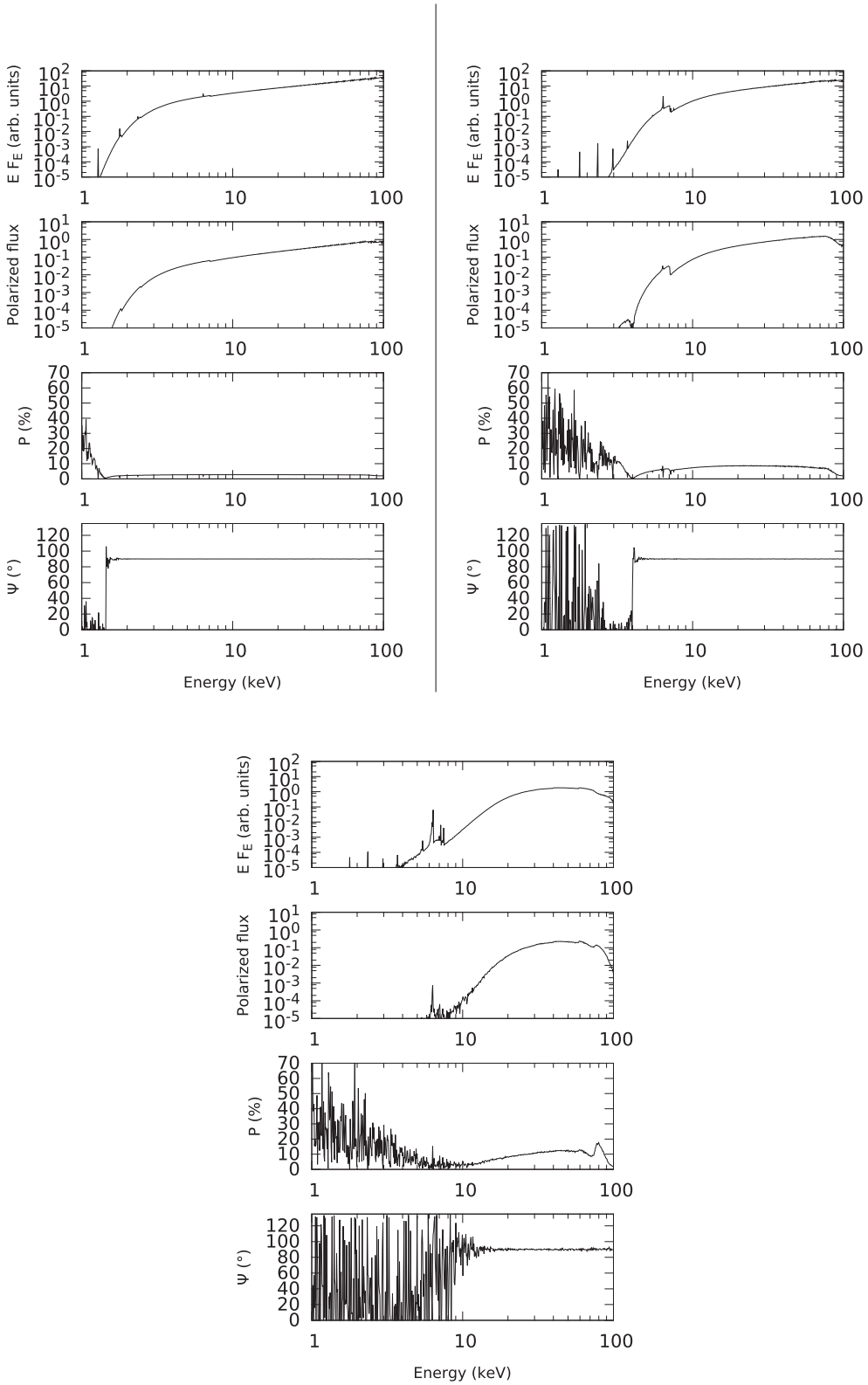

Figure C3. X-ray flux (F_E is energy flux at energy E), polarized flux, polarization degree and polarization position angle for a type 2 AGN without polar winds. Top-left: $n_{\mathrm{H_{torus}}} = 10^{23}$ atm cm^{-2}; top-right: 10^{24} atm cm^{-2}; bottom: 10^{25} atm cm^{-2}. See text for additional details about the model components. The input spectrum is polarized (2 per cent parallel polarization). Strong gravity effects are not included.

APPENDIX D

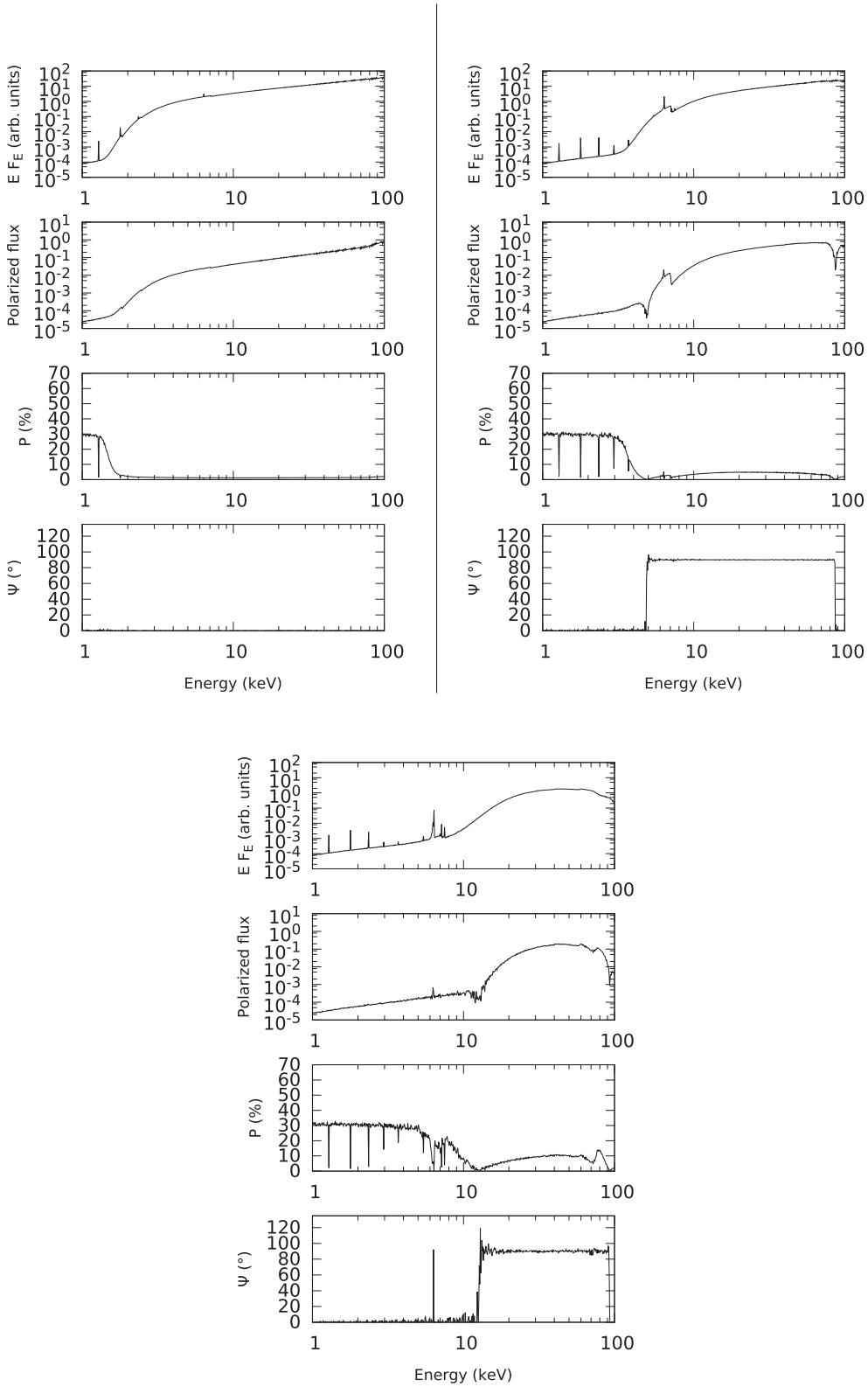

Figure D1. X-ray flux (F_E is energy flux at energy E), polarized flux, polarization degree and polarization position angle for a type 2 AGN with Compton-thin absorbing polar winds ($n_{\rm H_{wind}} = 10^{21}$ atm cm^{-2}). Top-left: $n_{\rm H_{torus}} = 10^{23}$ atm cm^{-2}; top-right: 10^{24} atm cm^{-2}; bottom: 10^{25} atm cm^{-2}. See text for additional details about the model components. The input spectrum is polarized (2 per cent perpendicular polarization). Strong gravity effects are not included.

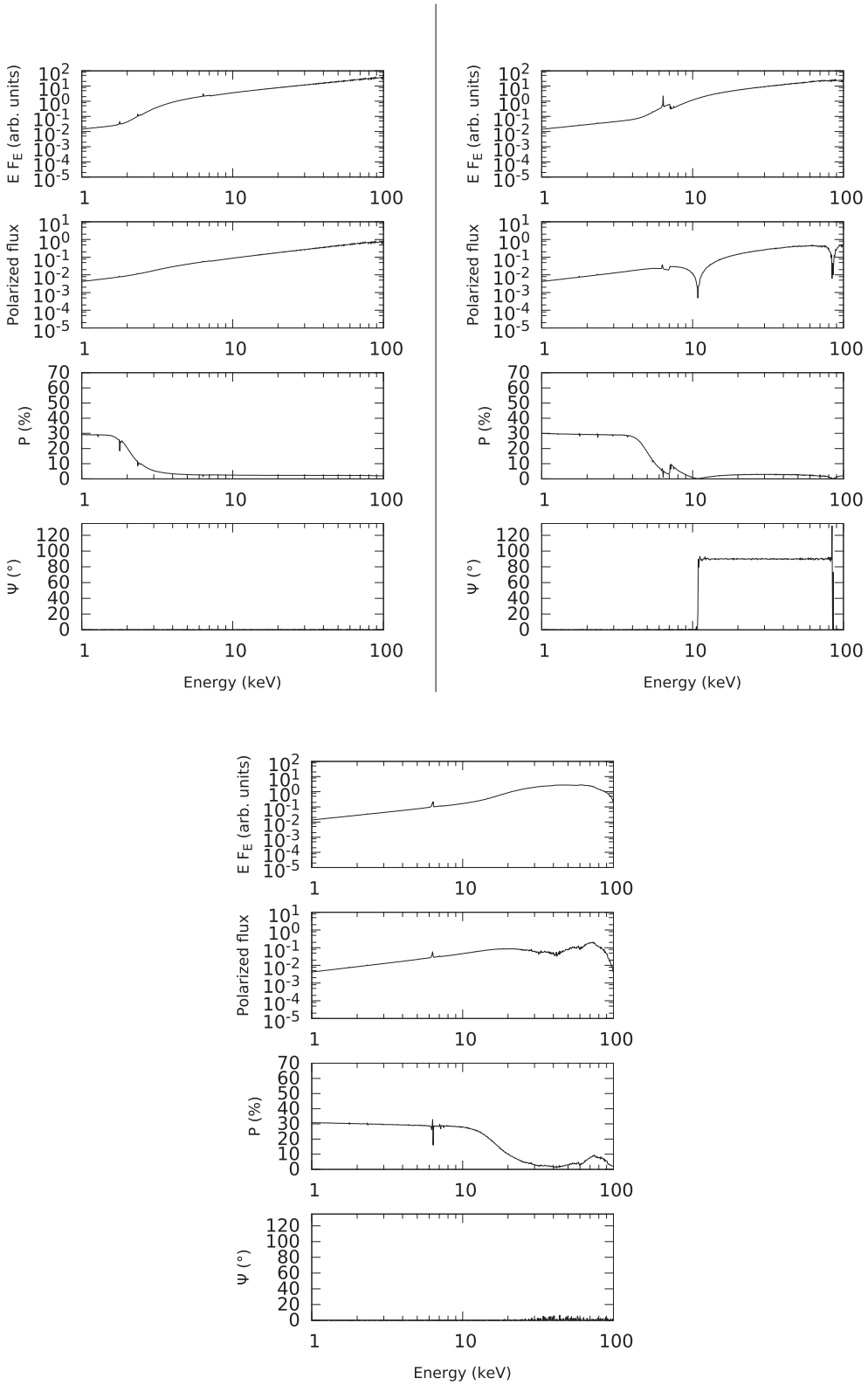

Figure D2. X-ray flux (F_E is energy flux at energy E), polarized flux, polarization degree and polarization position angle for a type 2 AGN with fully ionized polar winds. Top-left: $n_{\mathrm{H_{torus}}} = 10^{23}$ atm cm^{-2}; top-right: 10^{24} atm cm^{-2}; bottom: 10^{25} atm cm^{-2}. See text for additional details about the model components. The input spectrum is polarized (2 per cent perpendicular polarization). Strong gravity effects are not included.

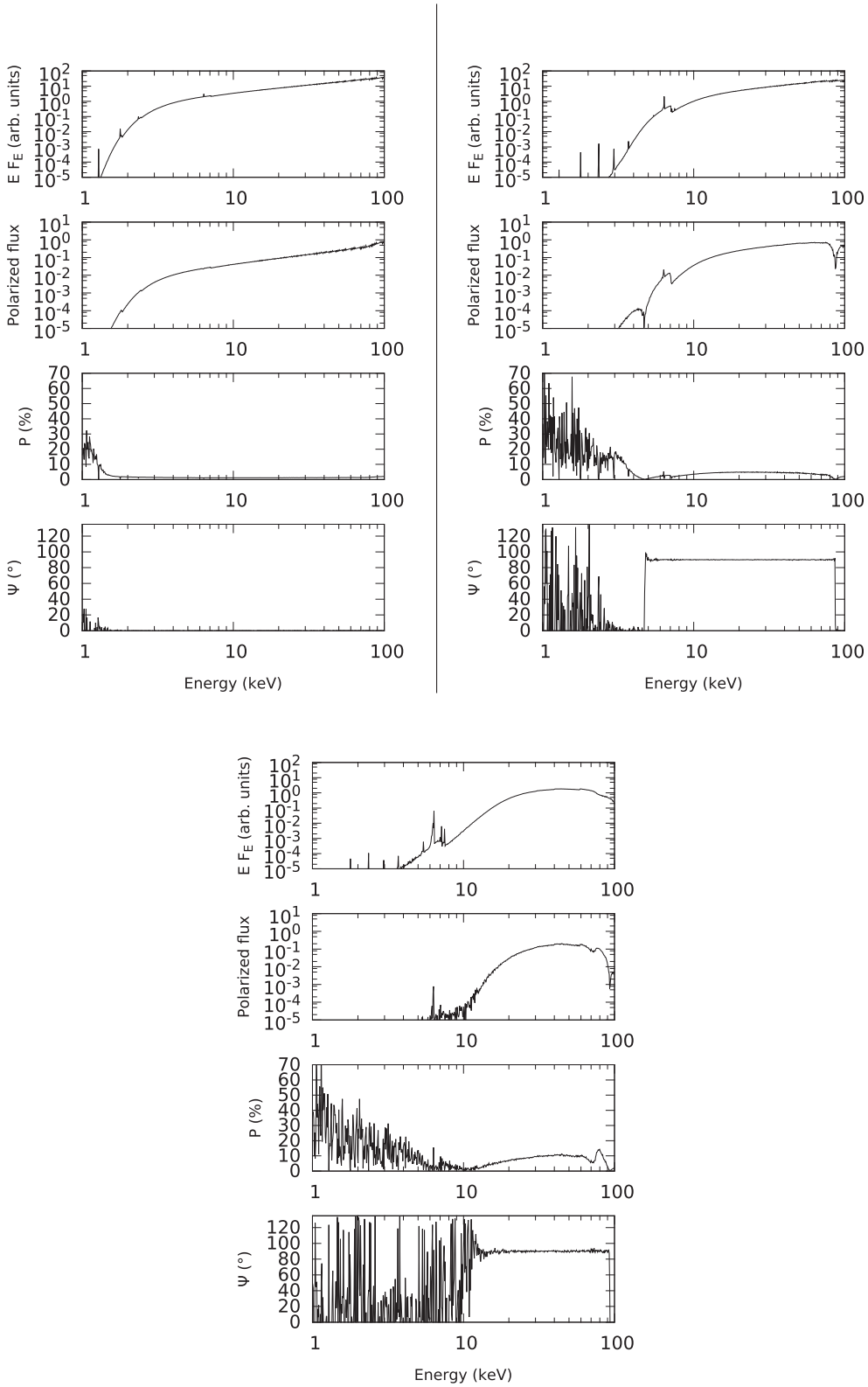

Figure D3. X-ray flux (F_E is energy flux at energy E), polarized flux, polarization degree and polarization position angle for a type 2 AGN without polar winds. Top-left: $n_{\mathrm{H_{torus}}} = 10^{23}$ atm cm^{-2}; top-right: 10^{24} atm cm^{-2}; bottom: 10^{25} atm cm^{-2}. See text for additional details about the model components. The input spectrum is polarized (2 per cent perpendicular polarization). Strong gravity effects are not included.

APPENDIX E

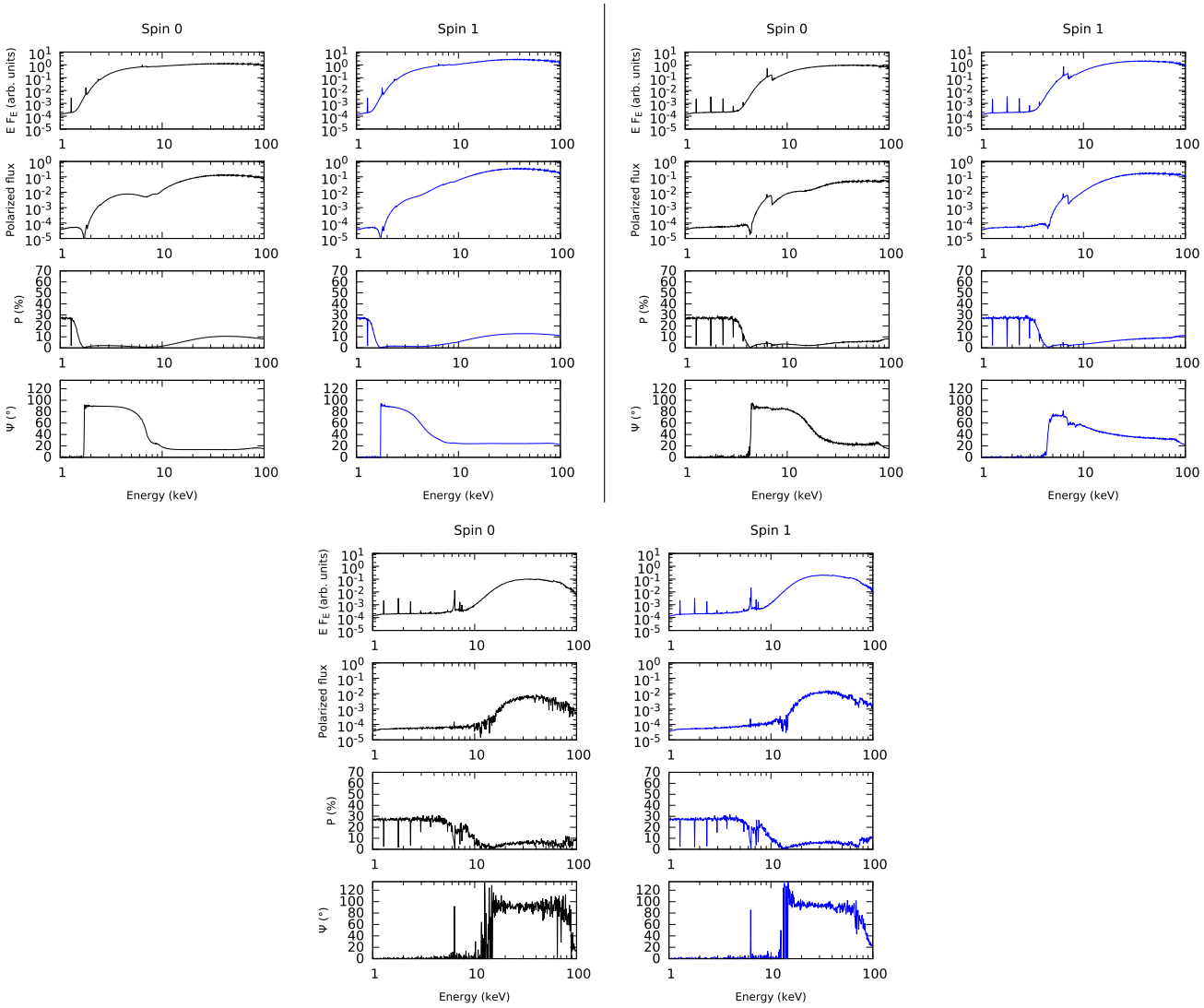

Figure E1. X-ray flux (F_E is energy flux at energy E), polarized flux, polarization degree and polarization position angle for a type 2 AGN with Compton-thin absorbing polar winds ($n_{\rm H_{wind}} = 10^{21}$ atm cm^{-2}). Top-left: $n_{\rm H_{torus}} = 10^{23}$ atm cm^{-2}; top-right: 10^{24} atm cm^{-2}; bottom: 10^{25} atm cm^{-2}. See text for additional details about the model components. The input spectrum is polarized (2 per cent parallel polarization), and GR effects are included (left-hand column: non-spinning Schwarzschild black hole; right-hand column: maximally spinning Kerr black hole).

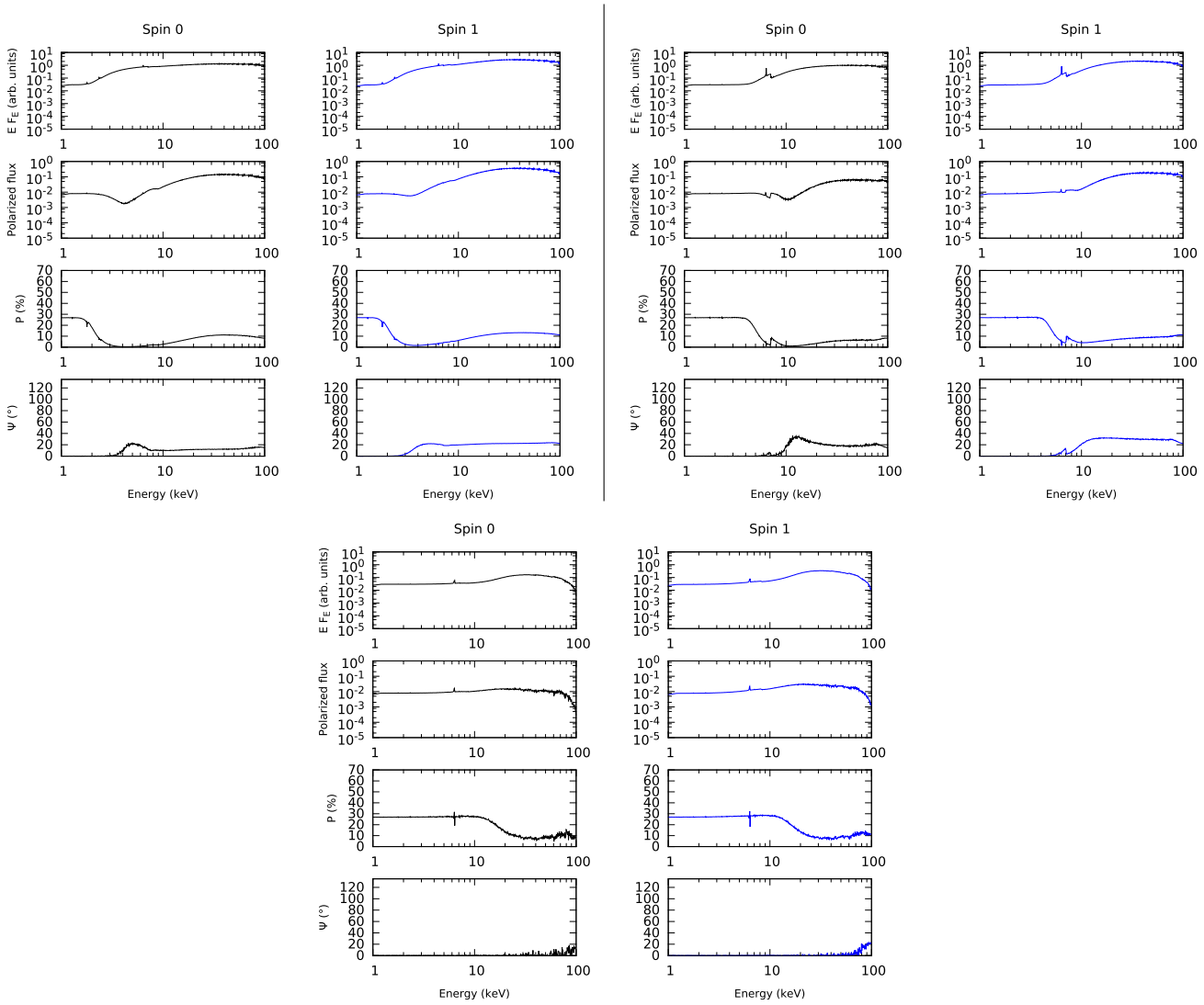

Figure E2. X-ray flux (F_E is energy flux at energy E), polarized flux, polarization degree and polarization position angle for a type 2 AGN with fully ionized polar winds. Top-left: $n_{\rm H_{torus}} = 10^{23}$ atm cm^{-2}; top-right: 10^{24} atm cm^{-2}; bottom: 10^{25} atm cm^{-2}. See text for additional details about the model components. The input spectrum is polarized (2 per cent parallel polarization), and GR effects are included (left-hand column: non-spinning Schwarzschild black hole; right-hand column: maximally spinning Kerr black hole).

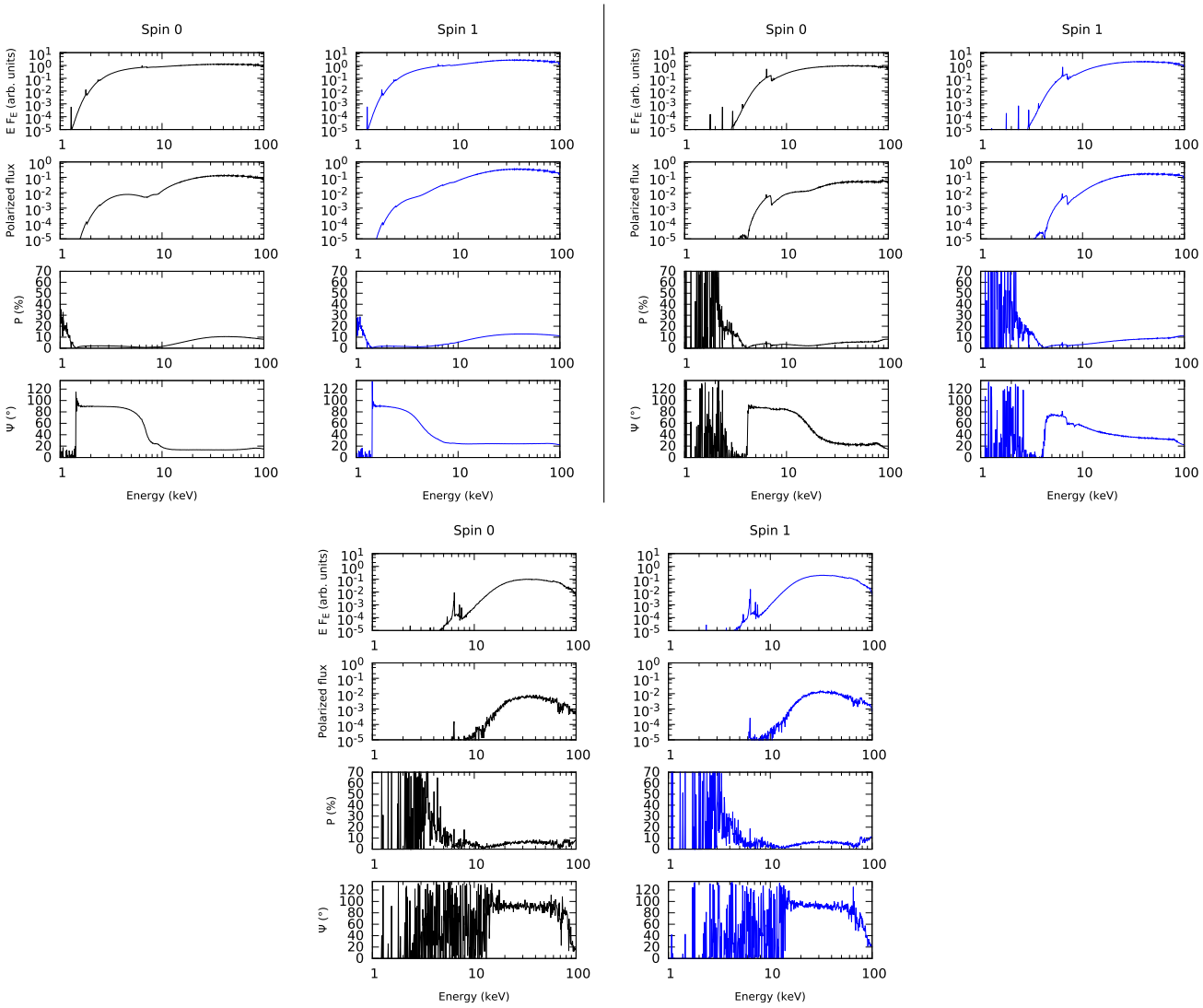

Figure E3. X-ray flux (F_E is energy flux at energy E), polarized flux, polarization degree and polarization position angle for a type 2 AGN without polar winds. Top-left: $n_{\rm H_{torus}} = 10^{23}$ atm cm^{-2}; top-right: 10^{24} atm cm^{-2}; bottom: 10^{25} atm cm^{-2}. See text for additional details about the model components. The input spectrum is polarized (2 per cent parallel polarization), and GR effects are included (left-hand column: non-spinning Schwarzschild black hole; right-hand column: maximally spinning Kerr black hole).

APPENDIX F

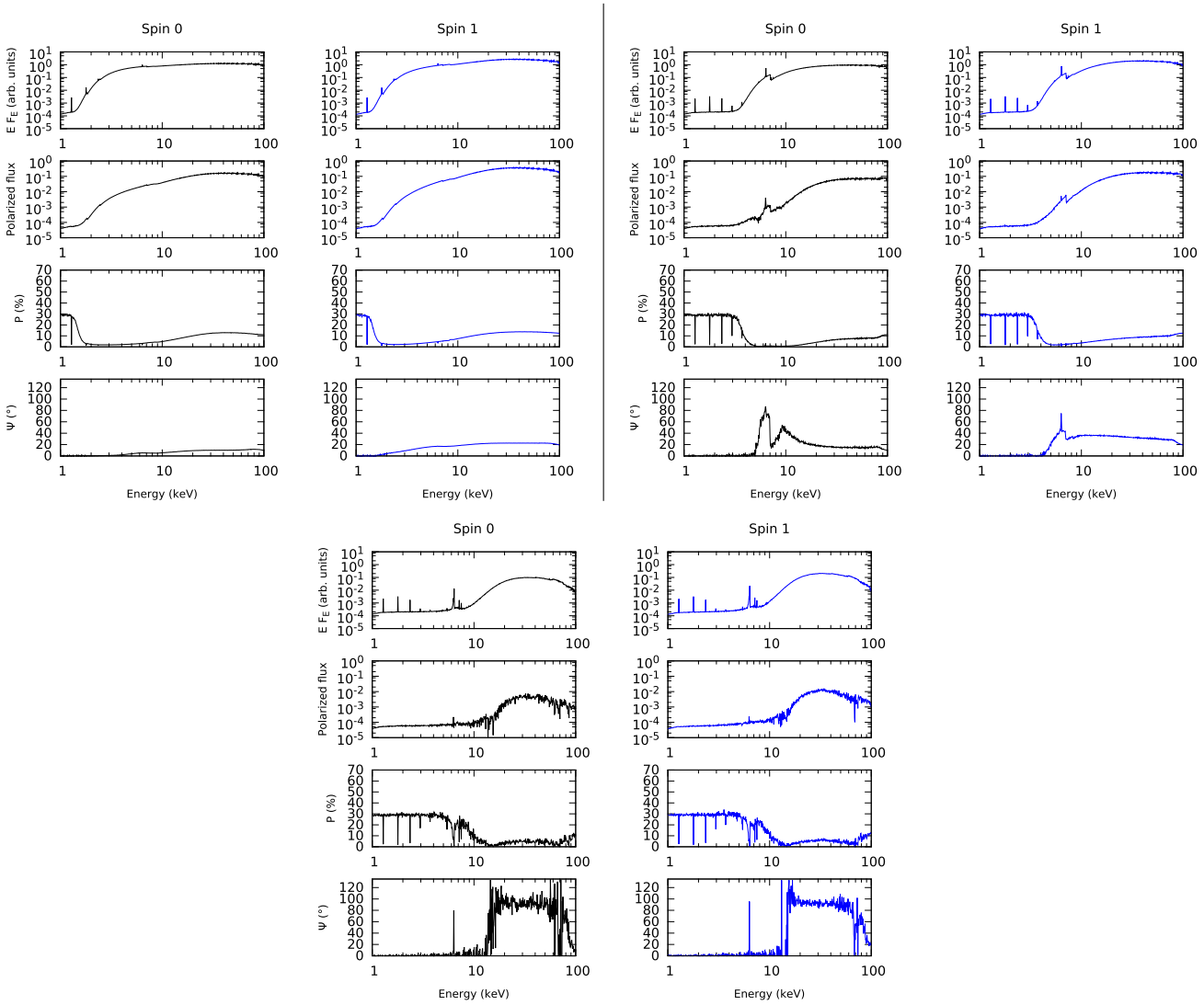

Figure F1. X-ray flux (F_E is energy flux at energy E), polarized flux, polarization degree and polarization position angle for a type 2 AGN with Compton-thin absorbing polar winds ($n_{\rm H_{wind}} = 10^{21}$ atm cm^{-2}). Top-left: $n_{\rm H_{torus}} = 10^{23}$ atm cm^{-2}; top-right: 10^{24} atm cm^{-2}; bottom: 10^{25} atm cm^{-2}. See text for additional details about the model components. The input spectrum is polarized (2 per cent perpendicular polarization), and GR effects are included (left-hand column: non-spinning Schwarzschild black hole; right-hand column: maximally spinning Kerr black hole).

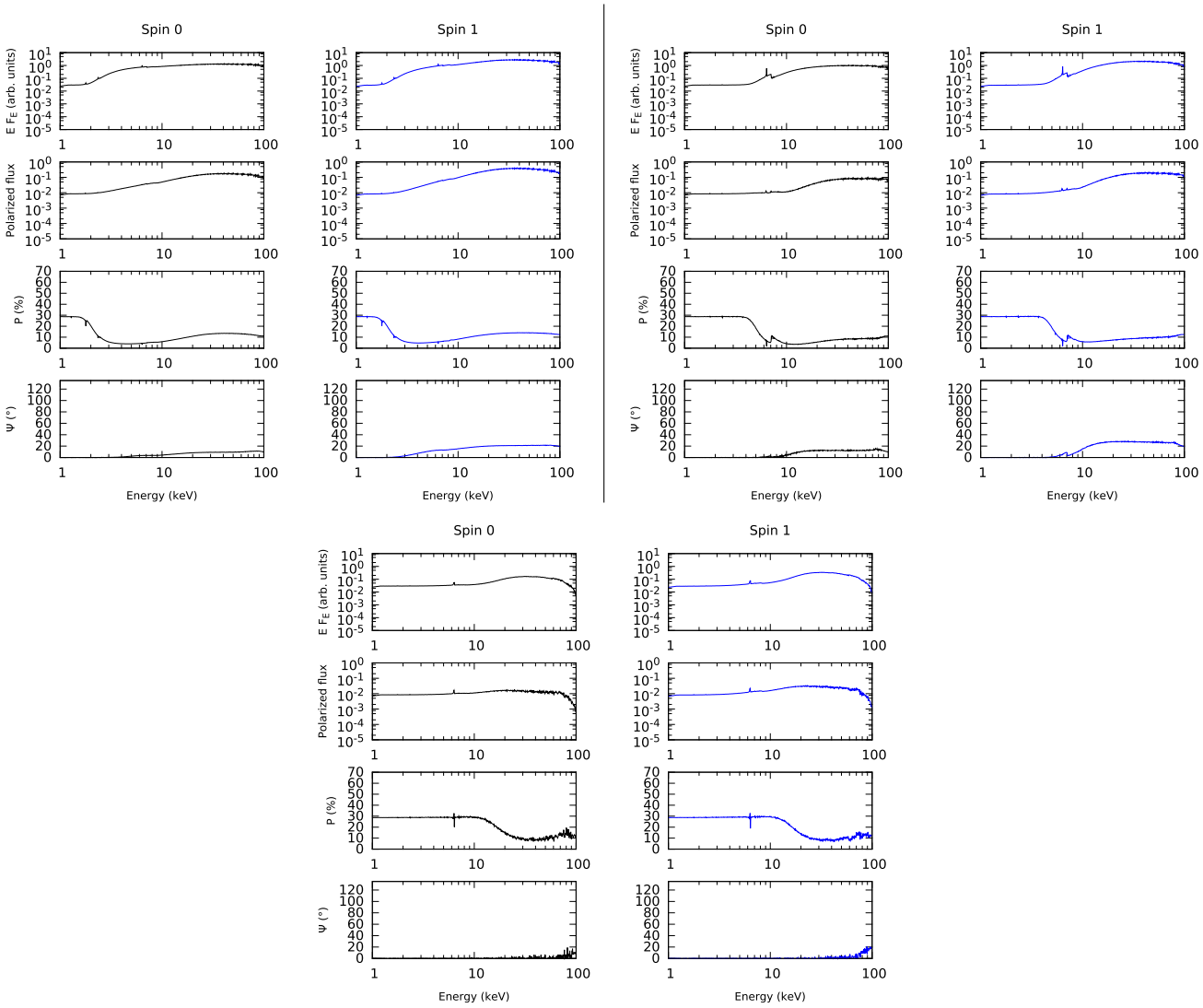

Figure F2. X-ray flux (F_E is energy flux at energy E), polarized flux, polarization degree and polarization position angle for a type 2 AGN with fully ionized polar winds. Top-left: $n_{\rm H_{torus}} = 10^{23}$ atm cm^{-2}; top-right: 10^{24} atm cm^{-2}; bottom: 10^{25} atm cm^{-2}. See text for additional details about the model components. The input spectrum is polarized (2 per cent perpendicular polarization), and GR effects are included (left-hand column: non-spinning Schwarzschild black hole; right-hand column: maximally spinning Kerr black hole).

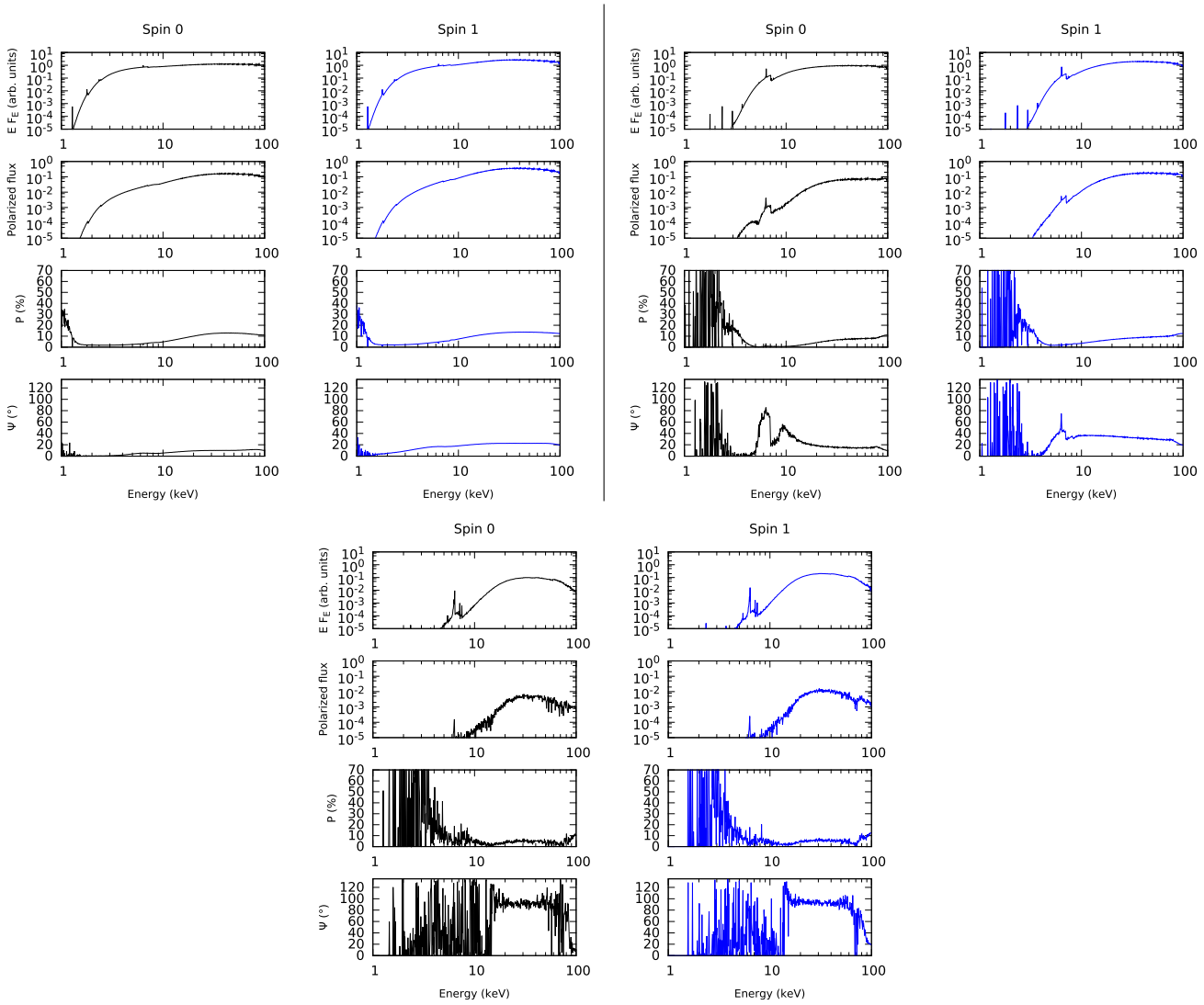

Figure F3. X-ray flux (F_E is energy flux at energy E), polarized flux, polarization degree and polarization position angle for a type 2 AGN without polar winds. Top-left: $n_{\rm H_{torus}} = 10^{23}$ atm cm^{-2}; top-right: 10^{24} atm cm^{-2}; bottom: 10^{25} atm cm^{-2}. See text for additional details about the model components. The input spectrum is polarized (2 per cent perpendicular polarization), and GR effects are included (left-hand column: non-spinning Schwarzschild black hole; right-hand column: maximally spinning Kerr black hole).

This paper has been typeset from a TEX/LATEX file prepared by the author.